Université de Montréal

3D adaptive Wiener filter to restore brain SPECT image with reference MRI

par

Wei Li

Institut de génie biomédical

Mémoire présenté à la Faculté des études supérieures
en vue de l'obtention du grade de Maîtrise ès sciences appliquées
en génie biomédical

Avril, 2005

Université de Montréal
Faculté des études supérieures

Ce mémoire intitulé :

3D adaptive Wiener filter to restore brain SPECT image with reference MRI

présenté par:

Wei Li

a été évalué par un jury composé des personnes suivantes :

Prof. Farida Cheriet, Ph.D., président rapporteur

Prof. Jean Meunier, Ph.D., directeur de recherche

Prof. Jean-Paul Soucy, Ph.D., codirecteur de recherche

Prof. Max Mignotte, Ph.D., membre du jury

Acknowledgement

I wish to take this opportunity to express my sincere thanks to my advisor, Prof. Jean Meunier, for his indispensable guidance, valuable suggestions, continuous encouragement and financial assistance in all the time of research and writing of this thesis. I have greatly benefited from not only his insights and enthusiasm on research, but also his unlimited patience and devotion to education.

I would like to thank my co-advisor, Dr. Jean-Paul Soucy, from University of Montreal Hospital (CHUM) and Montreal Neurological Institute (McGill University) for providing me raw data, having important discussions with me and helping me complete this thesis. I also want to thank Prof. Max Mignotte for his wonderful course, Image Processing, and his previous research works.

My colleagues of the laboratory of Vision give me lots of helps, specially, Elise Nguyen and Jean-François Laliberté. I want to say many thanks for being your colleague.

Finally, I am very grateful for my parents for their deep love. I believe that my father would be happy if he saw the finish of this thesis.

Abstract

Single Photon Emission Computed Tomography (SPECT) brain blood flow imaging is a routine diagnostic technique used in clinical settings to provide accurate assessments of a variety of neurological and psychiatric diseases, such as, epilepsy, dementias and other neurodegenerative affections, strokes, traumatic brain injury, etc.. However, brain SPECT imaging offers relatively low spatial resolution and often limited contrast, making it potentially difficult to interpret.

A restoration technique for enhancing image contrast and reducing noise using a 3D adaptive Wiener filter is presented in this work. The well-known Wiener filter is a global filter which is optimal in the sense that it minimizes the mean square error between the original image and the estimate. When the Wiener filter is applied to restore degraded images, *a priori* information about the point spread function (PSF) and the power spectrum of the original image and noise have to be available. Unfortunately, these information are generally unknown.

To overcome these limitations of the Wiener filter, we propose using a reference image to provide *a priori* information on the brain SPECT image and to track precisely the change of contrast and mottle. The reference image is produced by a higher resolution brain MRI scan of the same patient co-registered to the SPECT study. According to the characteristics of the brain SPECT imaging, we also assume that the PSF of the system is a Gaussian function with unknown standard deviation and the system noise is an additive white Gaussian noise (AWGN). The 3D adaptive Wiener filter then can automatically choose the best combination of its two parameters (the PSF width and the power spectrum density of noise) based on the contrast-mottle criterion to finally restore the SPECT image.

Tests are conducted with both synthetic SPECT images resulting from a digital Hoffman phantom and actual clinical SPECT cases. Our results show that the contrast of images is significantly improved by at least a factor of 2 while keeping amplification of noise at acceptable level.

***Key words**: restoration, Wiener filter, SPECT, MRI, image processing*

Résumé

L'imagerie SPECT du flot sanguin cérébral est un outil important dans le diagnostic et l'évaluation de maladies neurologiques et psychiatriques telles que l'épilepsie, les démences de type Alzheimer, les accidents vasculaires cérébraux, les lésions cérébrales traumatiques, etc.. Cependant, les images SPECT souffrent d'une pauvre résolution et d'un faible contraste qui peuvent rendre le diagnostic difficile pour les médecins.

Une méthode de restauration utilisant le filtre adaptatif de Wiener 3D a été proposée pour améliorer le contraste des images et réduire le bruit. Le filtre de Wiener est un filtre global bien connu qui est optimal dans le sens où l'erreur quadratique moyenne entre l'image originale et l'estimation est minimisée. Quand le filtre de Wiener est appliqué pour restaurer les images dégradées, des connaissances *a priori* sur la fonction de réponse impulsionnelle (PSF) du système de formation de l'image et les spectres de puissance de l'image original et du bruit sont nécessaires. Malheureusement, ces informations ne sont souvent pas disponibles.

Pour contourner ces problèmes, nous proposons d'utiliser une image de référence qui est capable de fournir une information *a priori* sur l'image SPECT du cerveau et de suivre précisément les changements du contraste et du bruit. L'image de référence est générée par le recalage d'une image IRM de ce même cerveau sur l'image SPECT. Nous supposons aussi que la PSF du système est une fonction Gaussienne avec un écart-type inconnu et le bruit est un bruit blanc gaussien additif (AWGN). Le filtre adaptatif de Wiener 3D peut alors choisir automatiquement la meilleure combinaison de ces deux paramètres (la largeur de la PSF et le spectre de puissance du bruit) basée sur un critère de contraste-bruit pour restaurer l'image SPECT.

Les tests sont faits sur des images SPECT synthétiques qui sont produites avec un fantôme numérique de Hoffman et de vraies images SPECT obtenues en clinique. Nos résultats indiquent que le contraste des images est amélioré au moins par un facteur 2. En même temps, l'amplification du bruit demeure acceptable.

Mot clés *: restauration, filtre de Wiener, SPECT, IRM, traitement d'images*

List of Contents

List of Figures

List of Abbreviations

1D	One Dimensional
2D	Two Dimensional
3D	Three Dimensional
ACR	American College of Radiology
AIR	Automated Image Registration
ARMA	Auto-Regressive Moving Average
AWGN	Additive White Gaussian Noise
CHUM	University of Montreal Medical Center
CSF	Cerebrospinal Fluid
DICOM	Digital Imaging and Communications in Medicine
EEG	Electroencephalogram
FWHM	Full Width at Half Maximum
GM	Grey Matter
MAP	Maximum *a Posteriori*
ML	Maximum Likelihood
MRI	Magnetic Resonance Imaging
NEMA	National Electrical Manufacturers Association
PSF	Point Spread Function
PMT	Photomultiplier Tube
SPECT	Single Photon Emission Computed Tomography
SID	Square Intensity Differences
WM	White Matter

Chapter 1

Introduction

Single Photon Emission Computed Tomography (SPECT) imaging of cerebral blood flow has been widely used in diagnosing brain diseases due to its ability to reveal abnormal regions of cerebral blood flow at a cost-efficient level. However brain SPECT images suffer from limited resolution and lower contrast compared to Magnetic Resonance Imaging (MRI) scans, which unfortunately can only provide anatomical information. The goal of this work is to improve the quality of the present SPECT images in clinic with the help of MRI data using a restoration approach. In this chapter, we will first introduce some general information about SPECT imaging, including a brief history, instrumentation, and examples of applications to clinical problems. We then address the issue of degradation that affects the quality of brain SPECT images in the second section. Section 1.3 contains a literature review of restoration techniques for dealing with degradation problem. A brief description about the Digital Imaging and Communications in Medicine (DICOM) standard that is widely used in the medical imaging community will be given in section 1.4. Finally, we will present the organization of the rest of this thesis.

1.1 SPECT imaging

1.1.1 The history of development of SPECT imaging

SPECT is routinely used to help diagnose a variety of diseases in every organ system of the human body. SPECT imaging uses a gamma camera to collect gamma rays emitted from a patient previously administered with a small dose of a radiotracer (usually composed of a carrier molecule determining the localization of the agent, and of a radioactive atom providing the detectable signal) and reconstructs 3D images based on

data thus collected. SPECT allows us to visualize functional information about a patient's body system or specific organ.

SPECT imaging is one of the most common tools in Nuclear Medicine. Nuclear Medicine has a complex and multifaceted heritage. Many scientists and researchers made their contributions to its development. Here we only mention those major evolutions in the history. Although the first emission computed tomography device, MARK IV, was developed by Kuhl and Edwards in 1963 [KE63], the foundation of Nuclear Medicine was laid down at the end of the 19th century and the beginning of the 20th century.

All began with the discovery of *X*-rays in 1895 by Roentgen, a German physics professor. While experimenting with electron beams in a gas discharge tube, he discovered some unknown (*X*) rays capable of producing an image on nearby photographic plates. Roentgen won the first Nobel Prize in physics in 1901. Roentgen's remarkable discovery precipitated one of the most important medical advancements in human history.

Henri Becquerel's discovery of natural radioactivity with uranium salts was in 1896 [Nob05]. This extraordinary discovery caused a real revolution in scientific thought and led to a new breakthrough in the understanding of the universe. He was therefore named "father of radioactivity".

Two years later, in 1898, Pierre and Marie Curie discovered the radioactive element polonium. They introduced the new term: "radioactive" [AE93]. After much very difficult and tiring work, the Curies were able to establish the chemical properties of polonium and those of another radioactive element, radium [CC1898]. Both polonium and radium were more radioactive than uranium. The Curies and Henri Becquerel were 1903 Nobel Laureates.

Lord E. Rutherford was a British physicist. He discovered three different kinds of radiation produced by uranium compounds in 1899 [BL04]. He then separated and named them alpha, beta and gamma radiation according to their penetrating abilities. He also proposed a model of the atomic nucleus. He was a 1908 Nobel Laureate.

In 1913 Frederick Soddy introduced the name "isotope". He obtained the 1921 Nobel Prize in Chemistry.

The first artificial radioactive isotopes were produced by Irene Curie, the daughter of Pierre and Marie, in 1934 (Noble Laureate in 1935). At the time, uses of radionuclides were only for some treatments(therapy) and metabolic tracer studies, rather than imaging, because more sophisticated, economical means to produce radioactive materials for widespread application in medicine, military and other industries were not available.

The widespread clinical use of Nuclear Medicine did not start until the mid of 20th century. The 1950s were a major milestone in Nuclear Medicine. In 1957, Walter Tucker's group at the Brookhaven National Laboratory invented the first iodine-132 and technetium-99m generator [SNM05]. Technetium-99m, a radioactive isotope of the man-made element technetium with a suitable half-life of about 6 hours, relatively low gamma energy (140-keV) and causing minimal radiation damage to body organs, thus, becomes the most widely used radioisotope.

In 1952, Hal O. Anger invented the first gamma camera, which included a pinhole collimator in front of a thallium-activated NaI(Tl) crystal (5/6" thick) and a large piece of photographic paper for in vivo studies of a tumor [Wag03]. In 1957, Anger replaced the film and screen with a NaI(Tl) crystal 4 inches in diameter followed by 7 photomultipliers. This is a truly revolutionary contribution to Nuclear Medicine as it is a stationary imaging system (versus Benedict Cassen's rectilinear motion of its scanner) that is simultaneously sensitive to the all radioactivity in a large field of view. Anger's design has not been dramatically improved and has only been evolving slowly to the present day. Modern Gamma cameras commonly use a lead collimator perforated with many parallel, converging or diverging holes instead of the original pin-hole configuration.

There were also important developments in image reconstruction, such as algorithm for compensation of photon attenuation and emission tomography. In 1963, Kuhl and Edwards presented the first tomography imaging system using detectors mounted around a patient's head, which became the precursor to SPECT. However these

images were of poor quality, so the technique was not widely accepted. In the same year, Alan M. Cormack, a nuclear physicist, developed mathematical algorithms to calculate internal attenuation values, which is very important for image reconstruction. In 1967, Godfrey N. Hounsfield developed image reconstruction algorithms for tomography using computers. The algorithms took into account the effects of photon attenuation and scatter. Both Cormack and Hounsfield were awarded the 1979 Nobel Prize in Physiology or Medicine.

The concept of the SPECT device was developed between 1974 and 1977 (J. Keyes and ass. and R. Jaszczak and ass.), while commercial production started in 1982 [Ste01].

Since then, SPECT imaging has become a major field in Nuclear Medicine [BPLM97] and the original single-headed camera has been replaced with two-, three- and four-headed scanners, or even full-ring systems (see Fig. 1), which provide faster scanning with superb resolution.

1.1.2 SPECT instrumentation

Most commercial SPECT equipments are based on the rotating gamma camera, either single- or multi-head, shown in Figure 1. A triple-headed SPECT system can provide three times as much data as single headed camera for the same data acquisition time, which results in higher resolution. No matter how the SPECT system is equipped, with one or multiple heads, the basic hardware components remain the same. A SPECT imaging system essentially includes:

* Collimator
* Detector/NaI (Tl) scintillation crystal
* Light guide
* Photomultiplier tube (PMT)
* Circuit for signal amplification and positioning
* Computer for data analysis and image reconstruction

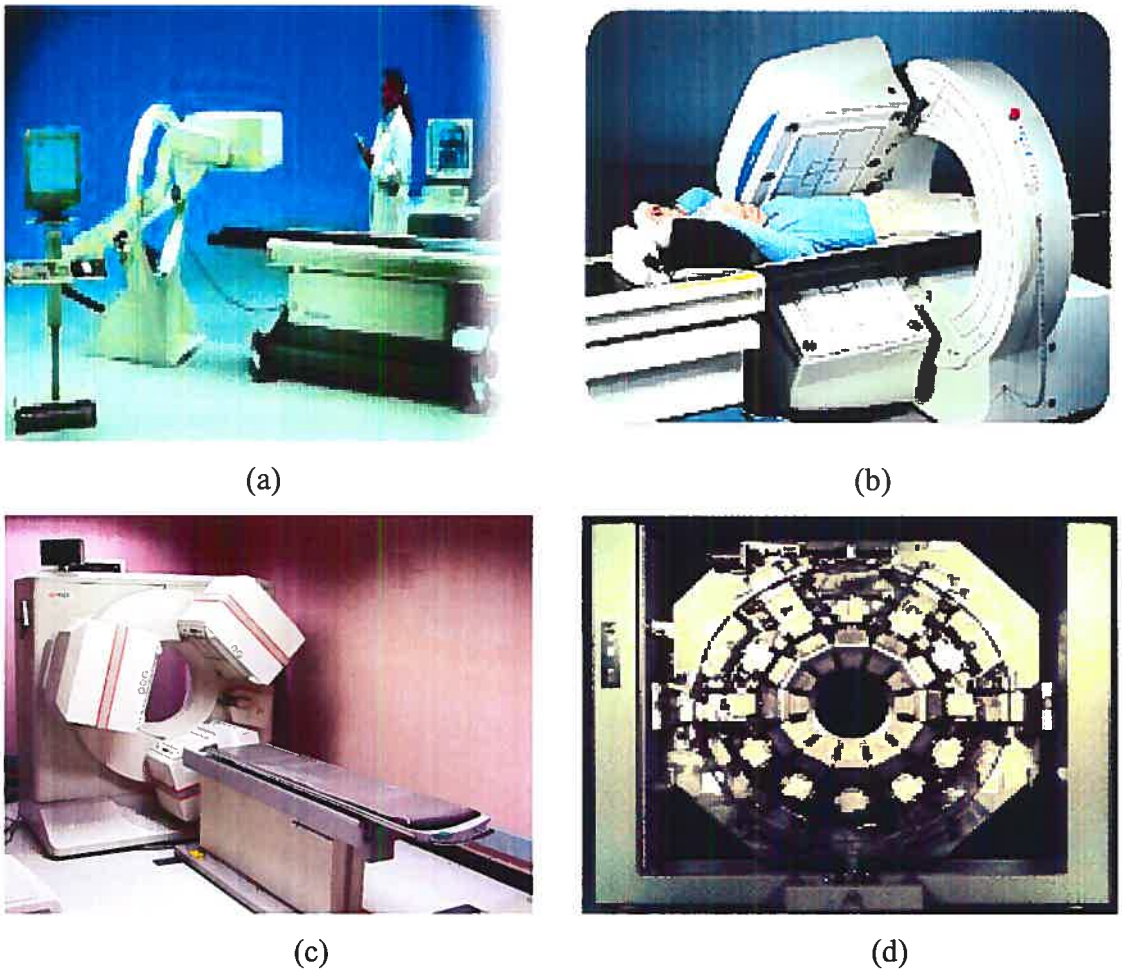

(a) (b)

(c) (d)

Figure 1: SPECT system with (a) One head. b) Bi-head. (c) Tri-head. (d) Full-ring detector.

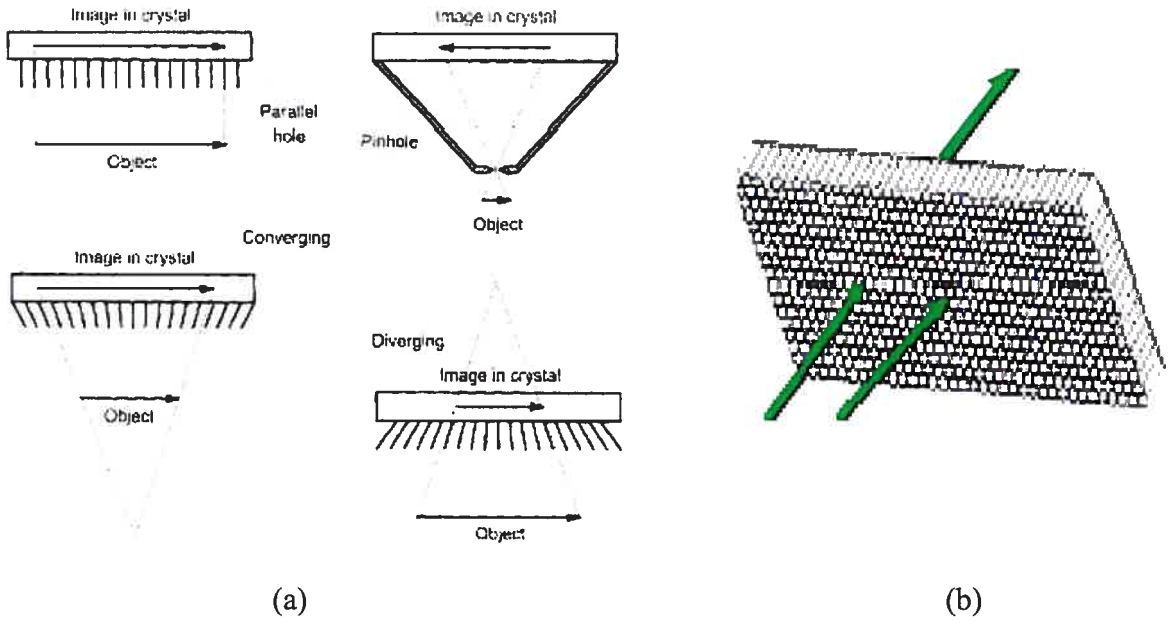

Figure 2: (a) Four types of collimator: parallel, pinhole, converging and diverging. (b) Parallel collimator.

The collimator is the first object that an emitted gamma photon encounters after exiting the body of a patient who is injected with a radioactive tracers, such as ^{99m}Tc, ^{67}Ga, or ^{111}In. The collimator is a crucial component of the gamma camera. Figure 2(a) shows four major types of collimators: parallel hole, pinhole, converging hole and diverging hole. The parallel-hole collimator is the most widely used, because the image size remains the same as the object size. This type of collimator selects photons having direction perpendicular to the surface of the scintillation crystal and absorbs all the rest of the radiation. Pinhole collimators offer higher magnification than parallel collimators and are used to magnify very small objects such as the thyroid by placing the object close to the pinhole, but at the cost of varying sensitivity depending on the location of the object and some distortion. The diverging and converging collimators can minimize and magnify the image. They create distortion in the images. The former is useful for imaging a large object with a small camera, and the latter, for imaging smaller objects.

After going through the collimator, the incident gamma photons are detected by the scintillation crystal that is the real gamma radiation detector. NaI(Tl) is the preferred

material due to its higher conversion efficiency – about 13% of the energy deposited in the crystal is emitted as visible light. The interaction of gamma ray photons with the crystal causes the release of the electrons that in turn interact with the crystal lattice to produce light photons. This phenomenon is called scintillation.

The light emitted by the crystal is then captured, amplified and localized by an array of photomultiplier tubes. As shown in Fig. 3(a), PMT array is attached to the back of the crystal. Each PMT consists of one photocathode and several dynodes (a typical photomultiplier tube has 10 to 12 dynodes). The photocathode converts light photons into electrons, and dynodes amplify the electrical signal at each step. Figure 3(b) describes the functions of a photomultiplier tube.

Usually, a gamma photon will be detected by more than one PMT. A position circuitry (Fig. 4(a)) is thus needed to determine the position of the scintillation event, based on the fact that the closer a PMT is to the scintillation event, the larger the output signal (Fig. 4(b)). The position of scintillation is finally determined by the calculation of the center of gravity of the outputs of the different PMTs.

In SPECT acquisition, a computer receives all incoming projection data (i.e. planar views acquired at multiple angles around the patient) and uses reconstruction algorithms to produce a final readable 3D image that depicts the 3D spatial distribution of gamma photo radioactivity within the patient.

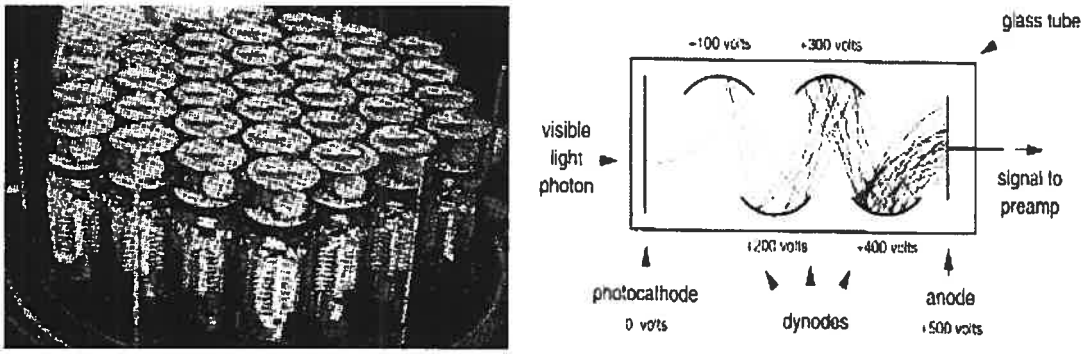

(a) (b)

Figure 3: (a) PMT array. (b) The functional diagram of one PMT

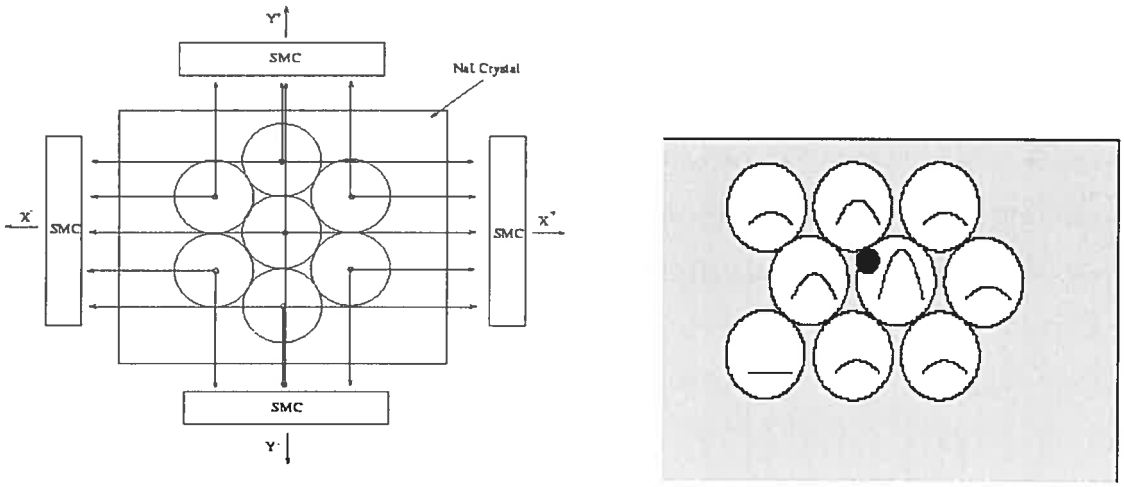

(a) (b)

Figure 4: (a) The functional diagram of the position circuitry. (b)The position of scintillation chosen by the position circuitry.

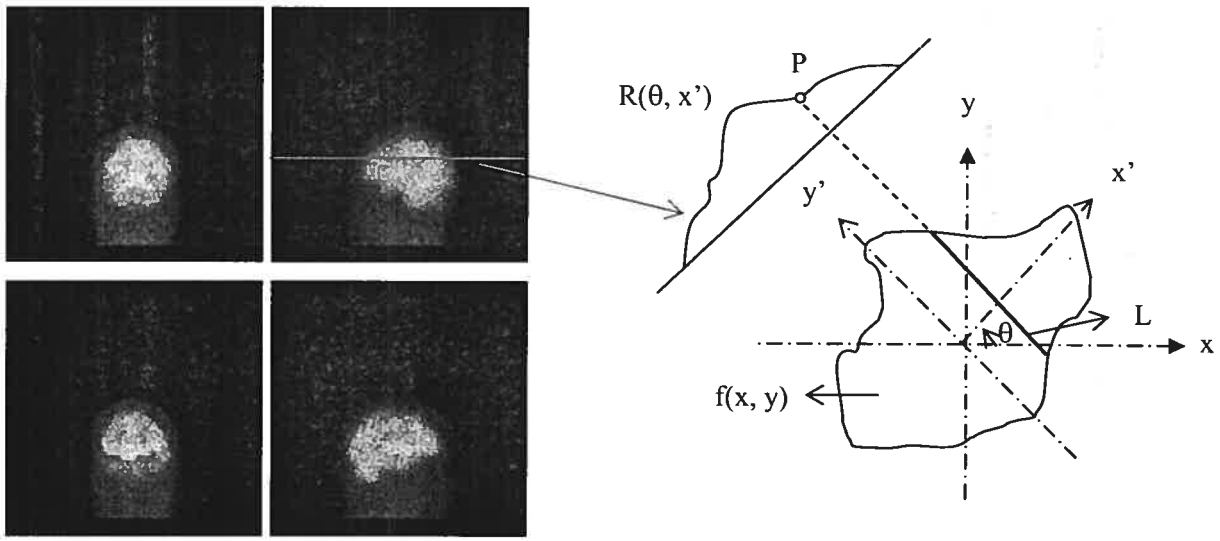

(a) (b)

Figure 5: (a) 3D SPECT data acquisition, a set of 2D projections (a total of 90 projections). (b) 1D projection of a plane at angle θ.

Before introducing SPECT image reconstruction, let's look at the data acquisition process. The SPECT data acquisition is a set of 2D projections, which are obtained by rotating the gamma camera heads around the patient at various angles and shown in Fig. 5(a). Mathematically, for parallel beam tomography, 1D projection of a

planar activity pattern $f(x, y)$ at angle θ can be described by the radon transform for a set of parameters (x', θ), which is the line integral through the image $f(x, y)$, where the line is positioned according to the value of (x', θ), shown in Fig. 5(b). The 1D projection function can be expressed by $R(x',\theta) = \int_{-\infty}^{\infty} f(x'\cos\theta - y'\sin\theta, x'\sin\theta + y'\cos\theta)dy'$. For example, the value at point P in Fig. 5(b) is the integral value along line L. The collection of Radon transforms of each slice of the object at all angles is called the sinogram (Fig. 6). A set of 2D sinograms form the raw data of a 3D SPECT image.

(a) (b)

Figure 6: (a) The collection of Radon transforms of a brain slice at all angles. (b) A slice of a brain SPECT image.

The most common reconstruction algorithm is filtered backprojection. It is based on the Fourier slice theorem, which tells us that the 1D Fourier Transform of the projection function at angle θ is identical to the spectrum along that angle θ in the frequency domain, i.e. the 2D Fourier Transform of the image. The principle of the filgtered backprojection for 2D image reconstruction is thus (a) taking 1D Fourier transforms of the projection function for each angle, (b)multiplying the result of the step (a) with a filter function $|\omega|$ (where ω is the radius in the polar coordinate system) in the frequency domain, (c) and then finding the inverse Fourier Transform. This algorithm can be easily extended to 3D volume. Without data filtering, the resultant reconstructed images would be extremely noisy and unreadable, so the filtered backprojection is actually used for the image reconstruction in most commercial SPECT systems. Figure 6(b) shows a slice of a brain SPECT image.

1.1.3 Application of brain SPECT imaging in clinic

Brain SPECT imaging using a variety of tracers (not just for evaluating blood flow) is a common application of SPECT imaging in the clinical world. It provides accurate assessment of regional cerebral functional activity that is important for the diagnosis of a variety of conditions. It can be used for instance in: (1) locating focal activation in epilepsy, (2) confirming and eventually specifying a clinical diagnosis of dementia, (3) giving supplementary information in addition to other imaging techniques (e.g. MRI or fMRI) to distinguish viable brain tumor from cerebral necrosis after radiation or chemotherapy, (4) allowing clinicians to clarify the nature of movement disorders such as Parkinson's disease. Some information on those diseases is listed below. Many other conditions can also be evaluated with above techniques.

Epilepsy, a condition where a subject suffers from recurrent seizures, is a common and serious neurological condition. At any one time between 1 in 140 and 1 in 200 people in the United Kingdom (at least 300,000 people) are being treated for epilepsy [MBWMB96] [WST98]. Each year, in a community of 250,000 people between 125 and 200 will develop epilepsy [FCMC02]. In the United States, the prevalence (the number of people with the disease at any one time) of adult-onset epilepsy is around 2 million [FCA2001], and incidence (new cases occurring in a population during a specific period, here one year) is 135,500 [FCA2001]. Accurate preoperative localization of the seizure focus is very important for effective surgical treatment of patients with medically intractable complex partial seizure. The investigation from Cascino *et al.* [CBMS04] shows ictal SPECT may be a reliable indicator of the ictal onset zone in patients' intractable partial epilepsy for which surgery could be considered.

Alzheimer's disease is the most common cause of dementia among people aged 65 and older. Scientists estimate that up to 4 million people currently suffer from the disease, and the prevalence doubles every 5 years beyond age 65 in the United States [ADERC05]. It is also estimated that approximately 360,000 new cases (incidence) will occur each year and that this number will increase as the US population ages [BGK98].

A recent study from the University of Texas Southwestern Medical Center by Frederick *et al.* published in May 2004 [FHRH04] showed that SPECT imaging may lead to early diagnosis of Alzheimer's disease. Researchers used SPECT to measure blood flow in the posterior cingulate cortex – an area of the brain that plays a part in orientation, sensory interpretation and vocabulary retention. The posterior cingulated sign allows doctors to differentiate early-stage Alzheimer's disease from other forms of dementia, such as frontotemporal disease.

Around 33,000 people are diagnosed annually with brain tumor (incidence) in the United States [ABTA00]. Evaluation of possible recurrence after therapy remains a significant clinical problem, and SPECT imaging with tracers such as ^{99m}Tc-MIBI can potentially help differentiate post-therapy damage from actual tumor recurrence. SPECT is not routinely used in the initial diagnosis of a brain tumor in the United States, but might complement information obtained from other scans to help doctors understand the effects of a tumor on brain activity and function.

The incidence and prevalence for Parkinson's disease are 54,927 [APTA00] and 1.5 million [NPF98], respectively, in the United States. Diagnosis can be quite difficult early on, even for specialized neurologists, and reports have accumulated recently on the potential of SPECT imaging with ligands targeting certain components of a specific neurotransmission system (the dopamine system) to allow for early, sensitive and specific diagnosis of this disease. For example, the findings from D. J. Tuite, MD, of Adelaide and Meath Hospital in Dublin [RSNA02] show that SPECT images are useful for early diagnosis of Parkinson's disease. They tested 50 patients using radiopharmaceutical agent ioflupane with SPECT. The sensitivity of the SPECT diagnosis achieves 98% and the specificity 97%. He mentions too, that positron-emission tomography (PET) is probably just as effective as SPECT but it is much more expensive and is not readily.

In addition, brain SPECT imaging is not only important for diagnosis, but also useful for case management, research, and follow-up of therapy efficacy such as potential neuroprotective and neurorestorative therapies for Parkinson's disease.

Since the total population of all those brain diseases is huge, it is very important to have an efficient and accurate tool for diagnosis. Although brain SPECT imaging has been employed for diagnosis for decades, researches by doctors and researchers are still on-going in order to provide earlier or more accurate diagnosis with SPECT.

1.2 Sources of degradation in SPECT imaging

SPECT imaging is widely used in diagnosis, follow-up of patients and therapeutic management. However, the images suffer from relatively poor spatial resolution and low contrast that can make it difficult for physicians to come up with an accurate interpretation for diagnosis, in particular, early diagnosis, i.e. when expected changes might be rather limited. In this section, we will introduce those major degrading effects in SPECT imaging.

The degradation of SPECT images comes from many sources: gamma photon attenuation, inherent blurring from collimator and scintillation detector, scattering effect, and statistical noise. These degradations make SPECT images blurry and noisy.

Attenuation is caused by the interaction of photons in the patient's body and other media on the path to the scintillation detector. The interaction of photons with matter causes four major effects [San03], photoelectric effect, Compton scattering (also known as incoherent scattering), coherent scattering, and pair production. The photoelectric effect takes place when a gamma photon strikes an orbital electron of the atom of materials (body or media) and the total energy of the gamma is spent in ejecting that electron from its orbit, as shown in Fig. 7(a). The photoelectric effect occurs when the energy of gamma ray is below 50 keV. Compton scattering is an interaction in which a part of the energy of the incident gamma photon being transferred to an orbital electron to cause its ejection, a new and lower energy gamma photon having the remainder of the original photon's energy is emitted with a direction different from that of the incident gamma photon, as shown in Fig. 7(b). Compton scattering is thought to be the dominant phenomenon for gamma rays in the intermediate energy range 100 keV to 10 MeV. Figure 7(c) shows coherent scattering effect, which occurs when the incident

gamma photon interacts with the whole atom. There is no internal energy exchange between the gamma photon and scattering atom, so the gamma photon just changes direction. Pair production is the case where a high energy gamma passes close enough to a heavy nucleus such that all the energy of the gamma is converted into the mass of an electron-positron pair. If the original gamma has at least 1.02 meV energy, the positron is then converted into two gamma photons with 0.51 keV energy each, shown in Fig. 7(d). Obviously, such energies are not encountered in clinical Nuclear Medicine.

Attenuation causes a reduction in the number of photon detected by the gamma camera, resulting in degradation of information about the distribution of the tracer within the body because attenuation is generally not uniform.

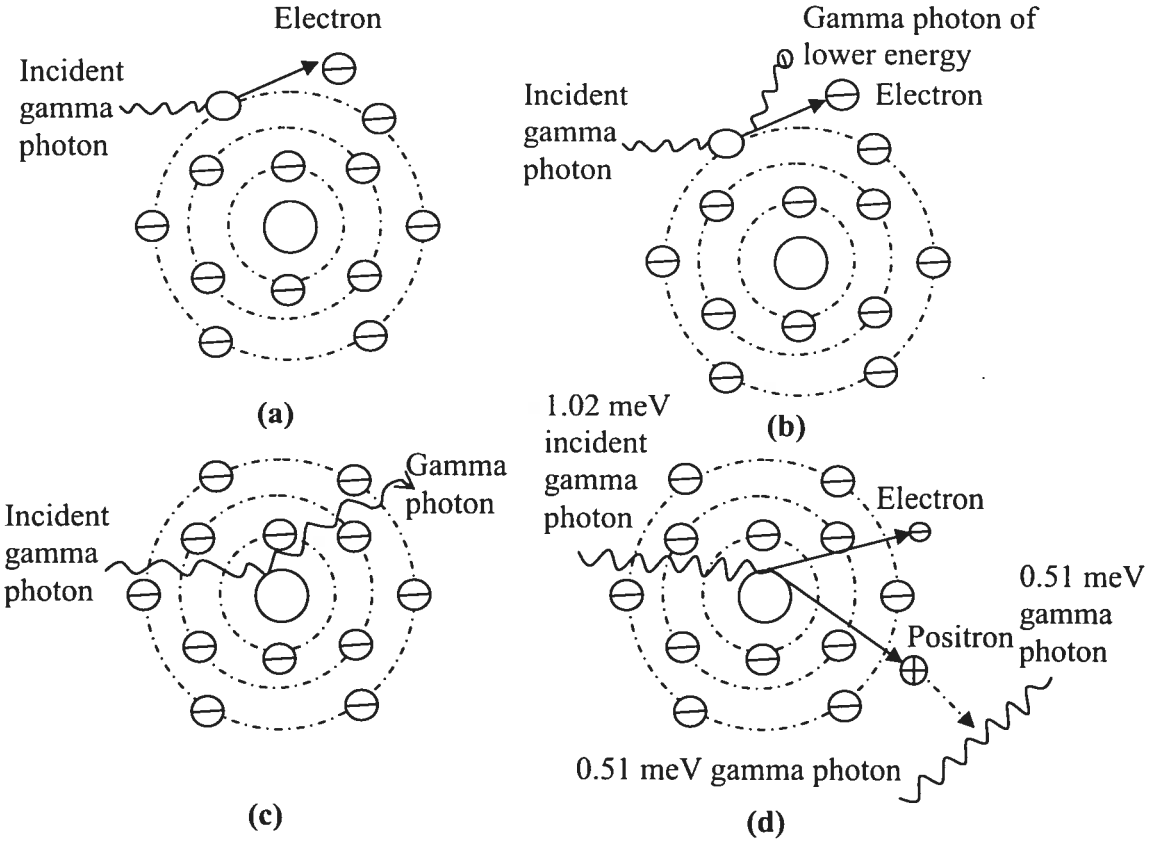

Figure 7: Four effects of attenuation. (a) Photoelectric effect. (b) Compton scattering. (c) Coherent scattering. (d) Pair production [AB05].

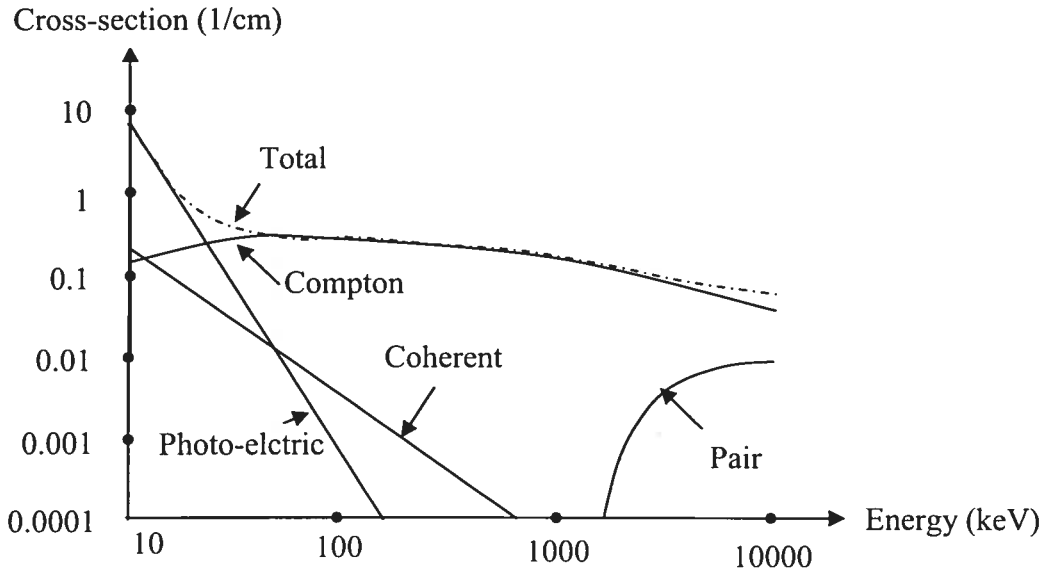

Figure 8: Differential cross-section for the photo-electric effect, Compton scattering, coherent scattering and pair production and total cross-section for water as a function of photon energy [San03].

Each of those effects, as mentioned, has a probably of occurrence which strongly depends on the photon energy and the property of material. Figure 8 shows the attenuation cross-section with respect to the photon energy. Due to low energy gamma photons used in SPECT, typically 100~300 keV, and to the fact that the human body is mainly made of water, photons experience more Compton scattering than the photoelectric interaction. The attenuation in SPECT is thus the main result of Compton scattering.

The collimator is a crucial component of the gamma camera, because collimation has the greatest effect on determining SPECT system spatial resolution and sensitivity, which are the main quality parameters of SPECT imaging system. Spatial resolution denotes the ability of the equipment to reproduce fine details, while sensitivity relates to the fraction of incident photons that is actually recorded by the imaging system. Resolution of a collimator is inversely related to its sensitivity. The resolution in Nuclear Medicine is usually expressed as the "full-width-at-half-maximum" (FWHM) amplitude. When a collimator has longer holes with a smaller diameter, it has better spatial resolution because the angle of acceptance is smaller and more scatter is rejected, while

its sensitivity is lower because fewer photons reach the scintillation detector. Figure 9(a) shows this feature. The collimator in Fig. 9(b) has opposite properties, higher sensitivity and lower resolution, because it has shorter holes with a wider diameter. Due to this characteristic, the design of a gamma camera for general purpose is a compromise between resolution and sensitivity. In other words, SPECT images are always blurred by the finite size and length of the collimator bores.

In addition to the effect of collimation, SPECT image resolution is also restrained by scintillation detector's response (the intrinsic resolution), and the distance of object to collimator. The intrinsic resolution varies with different manufacturers. The typical value of intrinsic resolution is between 3~5 mm (FWHM). In general, system resolution falls about 1 mm for each additional centimeter increased of a patient position from the face of a parallel-hole collimator. In Nuclear Medicine, resolution defines the degree of blurring along the boundaries between different regions of the image. The major factor limiting the resolution in SPECT is therefore the collimator-detector response blurring.

Besides collimation effect and the detector response blurring, detection sensitivity and the spatial resolution are also influenced by the dose of the agent used, the image voxel size, the number of projections, the acquisition time, and filtering process [Cat01].

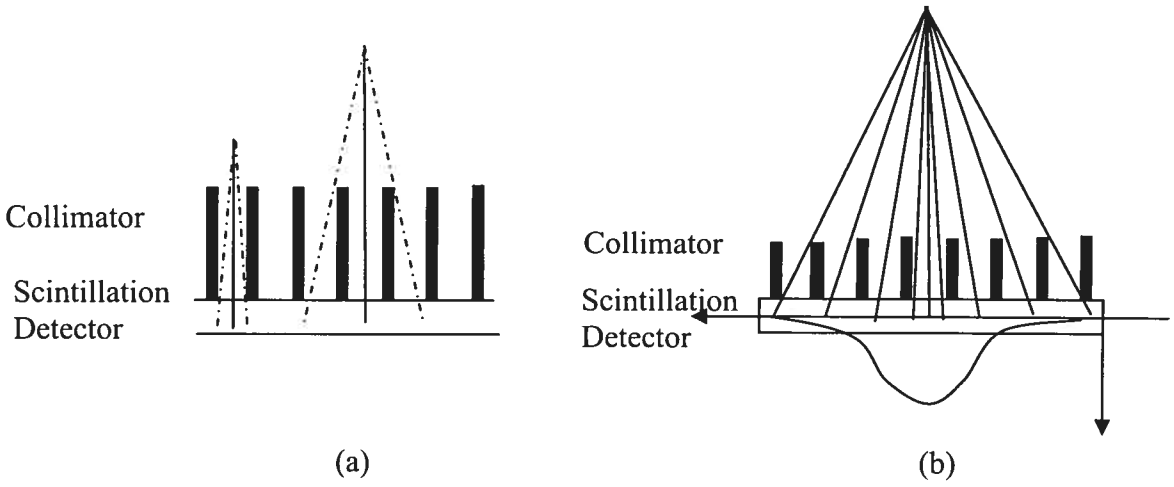

Figure 9: (a) Lower sensitivity and higher resolution collimator. (b) Higher sensitivity and lower resolution collimator.

Because the collimation blurring and the detector's intrinsic transform function are the two independent blurring sources, they can be analyzed as two sub-systems in series [MD79]. When the phenomenon of scattering is absent, the point spread function (PSF) for parallel-hole collimators is typically approximated as a Gaussian function [BB73] [GTMPB88]. The detector PSF depends on the precision of the positioning-logic circuits, and is usually modeled by a Gaussian function too.

The hypothesis that the PSF has Gaussian distributions for Fan-beam (diverging) collimator is confirmed by Pareto *et al.* [PPFJCR01]. Gaussian function is also used to simulate the intrinsic response of the detector for fan-beam collimator [FTG98].

Noise is the superposition of many factors, including photoelectric noise, electronic thermal noise, transmission noise and quantization noise. Since the detection of photons in SPECT is a Poisson process and the detection probability is very low, around 10^{-4}, measures of the projections include Poisson noise [San03]. Without attenuation correction, noise in SPECT is characterized by Poisson function. However, after application of the attenuation correction algorithm, the (slightly stronger) noise has a distribution similar to a Gaussian [AF99].

Some degradation is reduced or corrected by SPECT imaging design itself or image reconstruction procedure. For example, Compton scattering, can be reduced by using detectors with good energy resolution, which can distinguish the scattered photons from the original incident gamma photons. During the reconstruction, special mathematic algorithms, such as uniform algorithms, can compensate most attenuation effect. The present commercial SPECT systems frequently use the filtered backprojection reconstruction algorithm to process the acquired data for producing final images. Because the filtered backprojection algorithm cannot deal with photon interaction or detector characteristics, resolution degraded by the imaging process cannot be recovered by the reconstruction process. Although multi-detector system has been designed, which results in relative high spatial resolution and rapid imaging of the object, the typical spatial resolution of SPECT brain perfusion images can only achieve around 10 mm FWHM in the plane of the slice.

Thus, two problems, blurring and noise in the observed SPECT images, are commonly experienced in the context of image restoration for medical image processing.

1.3 Image restoration techniques overview

Altering acquisition and reconstruction strategies to account for a source of degradation is costly in terms of processing time, added complexity in imaging and processing, and / or enhancement other sources of degradation [Kin03]. As a result, actual SPECT images in clinic are usually noisy and have low contrast and spatial resolution when compared to those acquired with other imaging modalities. The objective of restoration is thus to recover as much information about the object being imaged from the degraded reconstructed image by modeling the imaging system and noise.

Image restoration is a field of digital image processing that attempts to reduce the effects of the PSF blurring and to remove the noise as much as possible. In other words, image restoration intends to achieve an improved image that is as close as possible to the real scene. Thus restoration techniques usually focus on modeling the degradation of imaging system, implementing the inverse process, and formulating a criterion to yield an optimal result. It should not be confused with another image improvement technique – enhancement, in which the chosen features are made more visible for further detection. Image restoration techniques share the same objective with image reconstruction processing and try to solve the same mathematical problem. However restoration is based on a full image, while reconstruction operates on a set of projection data.

A variety of restoration techniques have been developed, and also it exists a number of ways in classifying them. We classify these methods into two categories, restoration with *a priori* information and blind deconvolution without or with partial *a priori* information.

In the first category, we continue to classify them into linear restoration and non linear restoration methods. With linear methods, imaging system is modeled as a linear

shift-invariant system, which is a common model used in medical imaging systems. In other words, the degraded image is the convolution of the ideal image with the PSF of the system, plus superposition of additive noise. In non linear algebraic methods, the non linearity is introduced by either a nonlinear image formation and recording system model, or a linear shift-invariant system model with some constraints that produce non-linearity, e.g. non-negativity constraint – an image is formed always of positive intensities. This constraint is always true since the image is generated by the transport of radiant energy. Non linear properties may also come from the formulation of the restoration problem, for example, the use of complex optimization criteria.

Since there are multiple different restoration algorithms, we only introduce those methods that are the basis for others. For linear algebraic approach, a large class of restoration filters is derived based on least-squares criterion functions, considering either unconstrained or constrained approaches, which include inverse filtering, constrained least–square filter, Wiener filter, Tichonov-Miller, and maximum entropy method. For nonlinear approach, there are Van-Cittert, Landweber with positivity constrain, conjugate gradients form of Tichonov-Miller and stochastic (random) methods that employ maximum likelihood estimation and expectation-maximization algorithm.

Linear restorations

The linear shift-invariant system model in the spatial domain assumes that the observed image, represented as a stacked vector **g** and resulting from the imaging system, is equal to the product of a point spread function matrix **H** and the true image vector **f**, plus the noise vector **n** (see section 2.2).

Inverse filtering is an unconstrained linear restoration approach using least-square criterion, which assumes that the norm of the noise is as small as possible. In other words, it finds the estimate $\hat{\mathbf{f}}$ that minimizes the norm of the difference between the measured image **g** and the blurred estimate $\mathbf{H}\hat{\mathbf{f}}$. It is one of the simplest deconvolution methods. However, this method cannot tolerate any noise. In reality, noise is amplified due to the fact that the spectral properties of the noise are not taken

into account. As a consequence, this solution may not be implemented in practical applications where the data term is always affected by noise. The key problem of inverse filtering is that it treats both image structure and noise equally because it cannot distinguish them.

In mathematical terms, the restoration problem is ill-posed or ill-conditioned, that is, the problem cannot be uniquely solved. Small changes in the data can cause arbitrarily large changes in the results. In addition, the goals of image restoration, removing noise and deblurring (increasing contrast and resolution), are in conflict, because blur caused by any source is actually a form of bandwidth reduction of the image due to the image formation process, so a high-pass filter is needed to undo this part. On the other hand, noise is also composed of high frequencies, so a low-pass filter should be chosen to remove it. The ill-posed nature of restoration leads to more than one solution for the same system. Regularization methods are usually applied to solve ill-posed problems.

Regularization methods use *a priori* information for restoring degraded images. The key characteristic of regularization is a trade-off concept, that is, the choice of the penalty term, which balances between fidelity to measurements and to *a priori* information. Depending on the type of prior knowledge, there will be different mathematical expressions serving as a penalty term.

Constrained least-squares filter is a deterministic regularization method, which uses deterministic prior information about the original image. It is much more effective than the simple inverse filter. Hunt proposed this method that minimizes some linear operator on the object $\mathbf{Q}\hat{\mathbf{f}}$ with some other conditions, for instance, the norm of the noise signal [Hunt 73]. Using the method of Lagrange multipliers, the constrained least-square problem becomes to seek an estimate $\hat{\mathbf{f}}$ to minimize $\left\|Q\hat{\mathbf{f}}\right\|^2 + \alpha(\left\|g - \mathbf{H}\hat{\mathbf{f}}\right\|^2 - \left\|\mathbf{n}\right\|^2)$, where the parameter α is often obtained by an iterative method.

Wiener filter is a special case of constrained least-squares filters. From the viewpoint of implementation, Wiener filter is one of stochastic regularization approaches [BK97], which tries to minimize the mean square error between the original

image and the estimate subject to knowledge of signal and noise covariance matrices, $\mathbf{R}_f$ and $\mathbf{R}_n$, so it is also called least-mean-square filter. Here, the linear operator is chosen to be equal to $(\mathbf{R}_f)^{-1/2}(\mathbf{R}_n)^{1/2}$. The Fourier version of the Wiener filter can be very effective when the frequency characteristics of the image and additive noise are known (at least to some degree), and under the assumptions that both signal and noise covariance are stationary and independent. The Wiener filter is by far the most common deblurring technique used because it mathematically returns the best results and takes the shortest computational time to find a solution. The detail derivation of Wiener filter will be presented in Chapter 2.

The Tikhonov-Miller [Mil70] [PTVF92] restoration is linear and non-iterative in its original form. The method is based on a mean-square-error criterion and an energy bound that is the regularization parameter, the ratio of the noise power to the object power. Due to this bound, those spectral components outside the bandwidth of the PSF in the estimate $\hat{\mathbf{f}}$ will be suppressed. The solution may include negative values.

Introducing an appropriate cost function, such as entropy, is another way of regularization. The maximum-entropy method introduced by Jaynes in 1968 [Jay68] and Frieden in 1972 [Fri72] are widely used for astronomical image restoration. The principle of maximum entropy is a method for analyzing the available information in order to determine a unique epistemic probability distribution [Wik05]. If the object $\mathbf{f}$ is normalized to unit energy, then each f_i scalar value can be interpreted as a probability. Using constrained least-squares approaches, the maximum-entropy filter tries to minimize the negative of the entropy $\mathbf{f}' \ln \mathbf{f}$ subject to the constraint that is $\|\mathbf{g} - \mathbf{H}\mathbf{f}\|^2 = \|\mathbf{n}\|^2$ [AH77]. Maximum entropy helps suppress artificial oscillations but is sensitive to noise and slow when compared with other methods.

Non linear restoration

For non-linear methods, the results normally cannot be obtained by an analytical form. Instead, an iterative procedure is employed.

Van Cittert iterative deconvolution [Cit31], known as basic iterative deconvolution (BID), is based on the linear degrading system. In this technique, just like other iterative methods, the first step is to set the initial estimate to the measured image **g**. The basic idea of this algorithm is that if this first estimate $\mathbf{f}_1$ is correct, the difference of the measured image and the output $\mathbf{g}_1$ that is the result of blurring the first estimate $\mathbf{f}_1$ with the PSF, $\mathbf{g} - \mathbf{g}_1$, should be zero. If not, the correction might be made based on this difference. This algorithm is repeated until the error is below a threshold, or the update is no longer significant. Because this algorithm does not put any restraints on the fidelity to prior knowledge, it might result in severe noise amplification.

Iterative Tikhonov–Miller method is a modification of the analytical Tikhonov–Miller form. It adds an extra non-linear element property, positivity. Because the Tikhonov–Miller method includes a penalty term, it can thus effectively control noise amplification.

Many methods try to find the optimal value of the penalty term based on Tikhonov's regularization. For instance, the Conjugate Gradient Least-Square methods [HH94] use the number of iterations as a regularization parameter for the Tikhonov equation with no other regularization term.

Stochastic approaches are also used for image restoration. They are particularly effective when the blur function and the signal and noise power spectra can not be obtained. In stochastic approaches, the original image is assumed to be a realization of a random field, usually Gaussian or Markov. Maximum Likelihood (ML) and Maximum *a Posteriori* (MAP) approaches are specific types of stochastic methods.

Richardson [Fri72] and Lucy [Luc74] proposed the well-known Lucy-Richardson algorithm, which is derived from the maximum likelihood expression for a non linear system (with Poisson noise) through an iterative method. Lucy uses a correction term based on the ratio between the observed image and the estimate. A first guess must be specified, a constant for example, to start the iteration. This method is effective when the PSF and a little information about noise are known. However, this technique has a common problem just like other maximum likelihood methods, noise amplification, because it attempts to fit data as closely as possible.

A similar technique was proposed by Hunt in 1977 in which Maximum *a Posteriori* probability method was applied. The MAP solution differs from the ML solution solely because of the *a priori* information. The MAP estimate and the Wiener filter estimate in linear systems are the same on Gaussian densities [AH77]. The MAP problem is solved by the steepest descent method. An initial guess in MAP is usually made from a Wiener filter used as a linear approximation.

In the second category, blind deconvolution, both the true image and the PSF are estimated through an iterative approach using partial information about the imaging system. There are two main approaches to blind deconvolution of images, identifying the PSF separately from the estimation of the true image and simultaneously estimating the PSF and the true image [KH96]. Kundur *et al.* listed five blind deconvolution methods: *a priori* blur identification methods that fall into the first approach, Zero Sheet Separation methods, ARMA (Auto-Regressive Moving Average) Parameter Estimation methods, Nonparametric Deterministic Image Constrains Restoration and Nonparametric methods based on high order statistics that fall into the second approach.

An iterative approach has an advantage – an additional regularization obtained by ending iteration before convergence. On the other hand, iterative image restoration algorithms usually need a good estimate. For this purpose, the observed image is chosen for the first estimate. This is an obvious and frequently used way. However, when noise is present in the measured image, it may hamper the convergence of the algorithm.

In our work, we propose an adaptive Wiener filter, a new approach based on the Wiener filter, for improving SPECT images. Our approach overcomes the limitation of the Wiener filter and keeps its simplicity, stability, ability to remove noise, and efficiency of increasing contrast and resolution.

1.4 DICOM standard

In the medical imaging society, the DICOM standard is commonly used for the transmission and storage of digital medical images from the most common modalities in hospitals and clinics, such as SPECT and MRI. The standard was developed by the joint

committee of the American College of Radiology (ACR) and the National Electrical Manufacturers Association (NEMA) founded in 1983. The entire DICOM [DICOM04] standard consists of 18 parts. Image format is only one of several issues and is addressed in Part 10 of the standard. By convention, image files that are compliant with Part 10 of the DICOM standard are referred to as DICOM format file.

Unlike other medical image formats, a single DICOM file contains both head and image data. Using MRIcro [Ror04] software package, the DICOM files can be easily converted to other image formats applied frequently for medical image processing, such as the Analyze format that includes two separated components, header (.hdr) and image (.img) files.

The raw data we processed for this study are the DICOM format images.

1.5 Content of the rest of this thesis

We have reviewed the history of SPECT imaging, its application in clinic, degrading factors in SPECT imaging systems, different restoration methods that can improve degradation, and the DICOM standard for digital medical images. In Chapter 2, we will first derive Wiener filter mathematically, then we propose our adaptive Wiener filter. The third chapter describes the methodologies of the additive Wiener filter for restoration of SPECT images. Chapter 4 presents the experimental results on both Hoffman phantom and real SPECT images. The thesis is ended by the conclusion in the last chapter.

Chapter 2

Adaptive Wiener Filtering

2.1 Introduction

In chapter 1, many common linear and non linear image restoration approaches were reviewed. Among them, the Wiener filtering is the most common linear restoration technique due to its simplicity, capability of being computed in a straightforward and economical way and tolerance to noise.

The well-known Wiener filter is a global filter that is optimal in the sense that it minimizes the mean square error between the original image and the estimate. However, when we apply the Wiener filter to restore degraded images, *a priori* information, such as the PSF and the power spectra of the original image and noise, are needed. Unfortunately, these information are normally unknown.

In this work, we propose an iterative Wiener filter to overcome these limitations. Since we work in biomedical imaging, we assume that for the same patient, a higher resolution image (an anatomic image, such as, a MRI scan that uses magnets and radio waves and provides much higher details in the soft tissues, or a CT scan that uses x-ray and gives a good information of the bone structures) is acquired in addition to the SPECT image. We use this higher resolution MRI (or CT) volume with a set of image processing as our reference image to approximate the real scene – the "non-degraded SPECT image" that in fact never existed. Then the PSF and the power spectrum of noise are iteratively estimated based on a Gaussian PSF and Additive White Gaussian Noise (AWGN), as well as a criterion of image goodness – the contrast-mottle criterion.

In the following sections, we shall first formulate the restoration problem, then introduce the Wiener filtering algorithm, and finally present our adaptive method based on the Wiener filter.

2.2 Restoration problem formulation

Before formulating the restoration problem, we have to define the degradation model for SPECT imaging. This degrading system is assumed to be a linear shift-invariant system with additive noise [MM00], which is a common model used for most medical imaging systems. Although living systems are not linear, we can linearize them based on some reasonable assumptions, because such linear model will then allow us the luxury of borrowing from the field of linear systems theory, Fourier analysis, linear algebra, numerical analysis, and many other disciplines for clues as to useful inversion technique [AH77]. The focus of this thesis is image restoration; hence the system linearization will not be further discussed.

We start modeling a two dimensional imaging system. An imaging system is usually an image degradation process consisting of the input, the system, and the output, shown in Fig. 10.

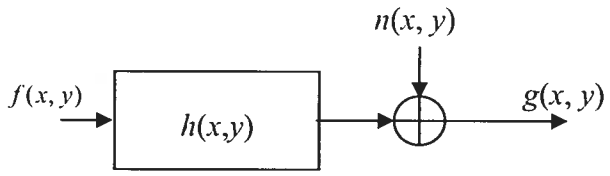

Figure 10: The block diagram of an imaging system.

A mathematical formula of this system may be expressed by:

$$g(x,y) = \sum_{k=1}^{M}\sum_{l=1}^{N} h(x-k, y-l) f(k,l) + n(x,y) = f(x,y) ** h(x,y) + n(x,y) \qquad (2.1)$$

where $f(x, y)$ and $g(x, y)$ represent an original and degraded $M \times N$ images respectively, $h(x, y)$ is the blur operator, also called the point spread function, and $n(x, y)$ denotes additive noise introduced by the imaging system. $**$ indicates two-dimensional convolution. Here we assume the image $f(x, y)$ and the function $h(x, y)$ are periodic both

in x and y directions with periods M and N, respectively. The resulting image $g(x, y)$ is also periodic with the same periods as $f(x, y)$ and $h(x, y)$.

Early classical techniques derive the Wiener filter from frequency-domain concepts. In this work, we introduce the algebraic approach derived by Gonzalez and Wintz [GW87] that allows us to compare the Wiener filtering with other restoration techniques. Therefore, we represent Eq. (2.1) in terms of a matrix-vector formulation, which is given by

$$\mathbf{g} = \mathbf{H}\mathbf{f} + \mathbf{n} \tag{2.2}$$

$$\mathbf{g} = \begin{bmatrix} g(0,0) \\ \vdots \\ g(0,N-1) \\ g(1,0) \\ \vdots \\ g(1,N-1) \\ \vdots \\ g(M-1,0) \\ \vdots \\ g(M-1,N-1) \end{bmatrix}_{MN\times 1} \quad \mathbf{f} = \begin{bmatrix} f(0,0) \\ \vdots \\ f(0,N-1) \\ f(1,0) \\ \vdots \\ f(1,N-1) \\ \vdots \\ f(M-1,0) \\ \vdots \\ f(M-1,N-1) \end{bmatrix}_{MN\times 1} \quad \mathbf{n} = \begin{bmatrix} n(0,0) \\ \vdots \\ n(0,N-1) \\ n(1,0) \\ \vdots \\ n(1,N-1) \\ \vdots \\ n(M-1,0) \\ \vdots \\ n(M-1,N-1) \end{bmatrix}_{MN\times 1} \tag{2.3}$$

where **g**, **f**, and **n** have the same meanings as for Eq. (2.1) except for the vector formulation. These vectors have MN (it means $M\times N$) dimensions obtained by stacking the rows (one can stack the columns too) of each of functions, $f(x, y)$, $g(x, y)$ and $n(x, y)$. The matrix **H** is $MN \times MN$ representing a superposition of blur operator and has special properties. These special properties are desirable for representing linear shift-invariant system and lead to the following special matrix structure:

$$\mathbf{H} = \begin{bmatrix} \mathbf{H}_0 & \mathbf{H}_{M-1} & \mathbf{H}_{M-2} & \cdots & \mathbf{H}_1 \\ \mathbf{H}_1 & \mathbf{H}_0 & \mathbf{H}_{M-1} & \cdots & \mathbf{H}_2 \\ \vdots & \vdots & \vdots & \ddots & \vdots \\ \mathbf{H}_{M-1} & \mathbf{H}_{M-2} & \mathbf{H}_{M-3} & \cdots & \mathbf{H}_0 \end{bmatrix}_{MN \times MN} \tag{2.4}$$

where **H** is called a $MN \times MN$ block-circulant matrix with $M \times M$ blocks and each sub-matrix $\mathbf{H}_i$ is itself a circulant $N \times N$ matrix. It is formed from the i-th row of the array $h(x,y)$ as follows:

$$\mathbf{H}_i = \begin{bmatrix} h(i,0) & h(i,N-1) & h(i,N-2) & \cdots & h(i,1) \\ h(i,1) & h(i,0) & h(i,N-1) & \cdots & h(i,2) \\ \vdots & \vdots & \vdots & \ddots & \vdots \\ h(i,N-1) & h(i,N-2) & h(i,N-3) & \cdots & h(i,0) \end{bmatrix} \tag{2.5}$$

where the array $h(x,y)$ is the blurring function. The matrix **H** has the circulant property because of the assumed periodicity of $h(x,y)$.

According to the degradation model, it is clear that the goal of restoration is to solve the inverse problem of Equation (2.1) or (2.2), in other words, to find the inverse transformation such that the original image can be recovered from the measured data:

$$\mathbf{f} = \mathbf{H}^{-1}(\mathbf{g} - \mathbf{n}) \tag{2.6}$$

The inverse transformation $\mathbf{H}^{-1}$ should exist and be unique, and noise characteristic should be known. If these conditions were satisfied in most applications, the restoration problem would not be a critical issue in image processing. However, the real word is always not the one we desire. For the situation where there is no inverse transformation (singular), which is not unusual, the restoration problem has no solution. Even if $\mathbf{H}^{-1}$ exists, it may be ill-posed. Hadamard first introduced the definition of ill-posedness in the field of partial differential equations [Had23]. A problem is well-posed when a solution exists, is unique and depends continuously on the initial data. It is ill-posed when it fails to satisfy at least one of these criteria. Andrews concluded that image

restoration is an ill-posed or ill-conditioned problem at best and a singular problem at worst [AH77].

Therefore, in the best case, there is usually no unique solution for restoration problem in view of noise and ill-conditioning. We thus use some prior knowledge to make an ill-posed problem well-posed, so the class of admissible solutions can be restricted. We will discuss them in the next subsection. It is important to keep in mind that the results for restoration problems are usually obtained in the optimal sense.

Notice that, even if the inverse transformation $\mathbf{H}^{-1}$ exists and is unique, and $\mathbf{n}$ is known, directly computing $\mathbf{H}^{-1}$ would be time consuming. For example, if we suppose $M = N = 512$, $MN = 262{,}144$ and $\mathbf{H}$ would be a 262,144 by 262,144 matrix to be inverted. Fortunately, the complexity of this problem can be reduced considerably by taking advantage of the circulant properties of $\mathbf{H}$ [GW87].

Since $\mathbf{H}$ is a block-circulant matrix, we can solve Equation 2.2 in a feasible way, by diagonalizing $\mathbf{H}$.

If $\mathbf{H}$ is a block-circulant matrix, according to [Hun73] we can write $\mathbf{H}$ as:

$$\mathbf{H} = \mathbf{E}\mathbf{D}\mathbf{E}^{-1} \text{ (with } \mathbf{E}\mathbf{E}^{-1} = \mathbf{E}^{-1}\mathbf{E} = \mathbf{I}) \tag{2.7}$$

$$\text{or } \mathbf{D} = \mathbf{E}^{-1}\mathbf{H}\mathbf{E} \tag{2.8}$$

where $\mathbf{D}$ is a diagonal matrix whose elements D(k, k) are related to the discrete Fourier transform of $h(x, y)$.

Multiplying both sides of Eq. (2.2) by $\mathbf{E}^{-1}$, and applying Eq (2.7), we get:

$$\mathbf{E}^{-1}\mathbf{g} = \mathbf{D}\mathbf{E}^{-1}\mathbf{f} + \mathbf{E}^{-1}\mathbf{n} \tag{2.9}$$

The product $\mathbf{E}^{-1}\mathbf{g}$ is an $MN \times 1$ vector, containing the stacked rows of the two dimensional discrete Fourier transform matrix $G(u, v)$ of $g(x, y)$. It is the same for the vectors $\mathbf{E}^{-1}\mathbf{f}$ and $\mathbf{E}^{-1}\mathbf{n}$.

Now the restoration problem becomes solving the following equation in the frequency domain, which avoids the calculation of the inverse matrix $\mathbf{H}^{-1}$. Eq. (2.9) can be written as:

$$G(u,v) = H(u,v)F(u,v) + N(u,v) \tag{2.10}$$

for $u = 0, 1, \ldots, M\text{-}1$ and $v = 0, 1, \ldots, N\text{-}1$.

In the following subsections, we shall introduce some criteria to obtain the solution for Eq. (2.10), the restoration problem.

2.3 Wiener filter

2.3.1 Introduction

The main technique used in order to transform the ill-posed problem into a well-posed one is the so-called "regularization procedure" [Mil70]. They usually use some *a priori* information for the derivation of a solution. The Least-squares criterion is one of those techniques that will give a unique solution and possesses simplicity. Two approaches, unconstrained and constrained, could be considered to solve the least-squares restoration problem. We derive these two approaches using Gonzalez and Wintz formulation [GW87].

2.3.2 Inverse filter – least-squares unconstrained restoration

We will first introduce the solution for unconstrained restoration problems. This method will lead to the inverse filtering, which is not our goal but has some important relation with Wiener filtering.

We can rewrite Eq. (2.2) to express the noise term:

$$\mathbf{n} = \mathbf{g} - \mathbf{H}\mathbf{f} \tag{2.11}$$

The unconstrained criterion here is to find the estimate $\hat{\mathbf{f}}$ of the original $\mathbf{f}$ to minimize $\left\|\mathbf{g} - \mathbf{H}\hat{\mathbf{f}}\right\|^2$ in a least-square sense under the assumption that the norm of the noise term is as small as possible. This problem can be therefore expressed by minimizing the criterion function:

$$J(\hat{\mathbf{f}}) = \left\|\mathbf{g} - \mathbf{H}\hat{\mathbf{f}}\right\|^2 \tag{2.12}$$

with respect to $\hat{\mathbf{f}}$, where, $\left\|\mathbf{g}-\mathbf{H}\hat{\mathbf{f}}\right\|^2 = (\mathbf{g}-\mathbf{H}\hat{\mathbf{f}})^T(\mathbf{g}-\mathbf{H}\hat{\mathbf{f}})$, the square norm of $(\mathbf{g}-\mathbf{H}\hat{\mathbf{f}})$. It is noted that $\hat{\mathbf{f}}$ is not constrained by other requirements except that it is required to minimize Eq. (2.12).

Minimization of Eq. (2.12) is obtained by differentiating the function J with respect to $\hat{\mathbf{f}}$. By setting the result to zero we get the following equation:

$$\hat{\mathbf{f}} = (\mathbf{H}^T\mathbf{H})^{-1}\mathbf{H}^T\mathbf{g} = \mathbf{H}^{-1}(\mathbf{H}^T)^{-1}\mathbf{H}^T\mathbf{g} = \mathbf{H}^{-1}\mathbf{g} \tag{2.13}$$

Replacing $\mathbf{H}^{-1}$ in the above equation by Eq. (2.7), we have:

$$\hat{\mathbf{f}} = (\mathbf{E}\mathbf{D}\mathbf{E}^{-1})^{-1}\mathbf{g} = \mathbf{E}\mathbf{D}^{-1}\mathbf{E}^{-1}\mathbf{g} \tag{2.14}$$

Multiplying both sides of Equation (2.14) by $\mathbf{E}^{-1}$ as we did previously, yields:

$$\mathbf{E}^{-1}\hat{\mathbf{f}} = \mathbf{D}^{-1}\mathbf{E}^{-1}\mathbf{g} \tag{2.15}$$

Using notations in the frequency domain, the above equation is expressed by:

$$\hat{F}(u,v) = \frac{G(u,v)}{H(u,v)} \tag{2.16}$$

which is refereed to as the inverse filter method.

2.3.3 Wiener filter least-squares constrained restoration

In constrained image restoration, we will first define a matrix $\mathbf{Q}$ with appropriate dimension and then choose an estimate $\hat{\mathbf{f}}$ to minimize $\left\|\mathbf{Q}\hat{\mathbf{f}}\right\|^2$, subject to the constraint $\left\|\mathbf{g}-\mathbf{H}\hat{\mathbf{f}}\right\|^2 = \|\mathbf{n}\|^2$. In other words, we seek an $\hat{\mathbf{f}}$ that minimizes the following criterion function:

$$J(\hat{\mathbf{f}}) = \left\|\mathbf{Q}\hat{\mathbf{f}}\right\|^2 + \alpha\left(\left\|\mathbf{g}-\mathbf{H}\hat{\mathbf{f}}\right\|^2 - \|\mathbf{n}\|^2\right) \tag{2.17}$$

where α is a constant called the Lagrange multiplier.

Minimization is carried out by differentiating Eq. (2.17) with respect to $\hat{\mathbf{f}}$ and setting the result equal to zero:

$$\frac{\partial J(\hat{\mathbf{f}})}{\partial \hat{\mathbf{f}}} = 2\mathbf{Q}^T\mathbf{Q}\hat{\mathbf{f}} - 2\alpha\mathbf{H}^T(\mathbf{g} - \mathbf{H}\hat{\mathbf{f}}) = \mathbf{0} \tag{2.18}$$

We obtain the solution for the general constrained restoration problem by solving (Eq. 2.18) for $\hat{\mathbf{f}}$. This is given by:

$$\hat{\mathbf{f}} = \left(\mathbf{H}^T\mathbf{H} + \gamma\mathbf{Q}^T\mathbf{Q}\right)^{-1}\mathbf{H}^T\mathbf{g} \tag{2.19}$$

where $\gamma = 1/\alpha$ is chosen to satisfy the constraint $\left\|\mathbf{g} - \mathbf{H}\hat{\mathbf{f}}\right\|^2 = \|\mathbf{n}\|^2$.

Wiener has derived an optimal solution based on the statistic of the image and noise features, mean and correlation. If each element of **f** and **n** is considered as a random variable, we can define two correlation matrices:

$$\mathbf{R}_\mathbf{f} = E(\mathbf{f}\mathbf{f}^T) = \begin{bmatrix} E(f_0f_0) & E(f_0f_1) & \cdots & E(f_0f_{MN-1}) \\ E(f_1f_0) & E(f_1f_1) & \cdots & E(f_1f_{MN-1}) \\ \vdots & \vdots & \ddots & \vdots \\ E(f_{MN-1}f_0) & E(f_{MN-1}f_1) & \cdots & E(f_{MN-1}f_{MN-1}) \end{bmatrix} \tag{2.20}$$

$$\mathbf{R}_\mathbf{n} = E(\mathbf{n}\mathbf{n}^T) = \begin{bmatrix} E(n_0n_0) & E(n_0n_1) & \cdots & E(n_0n_{MN-1}) \\ E(n_1n_0) & E(n_1n_1) & \cdots & E(n_1n_{MN-1}) \\ \vdots & \vdots & \ddots & \vdots \\ E(n_{MN-1}n_0) & E(n_{MN-1}n_1) & \cdots & E(n_{MN-1}n_{MN-1}) \end{bmatrix} \tag{2.21}$$

where $E(\cdot)$ denotes the expected value operation. Since the elements of **f** and **n** are real, $E(f_if_j) = E(f_jf_i)$ and $E(n_in_j) = E(n_jn_i)$, the matrices $\mathbf{R}_\mathbf{f}$ and $\mathbf{R}_\mathbf{n}$ are real and symmetric with all non-negative eigenvalues. Andrews and Hunt showed that $\mathbf{R}_\mathbf{f}$ and $\mathbf{R}_\mathbf{n}$ can be made to approximate block-circulant matrices and can be diagonalized by the matrix **E** [AH77]. It leads to the Fourier transform of the correlations, $\mathbf{R}_\mathbf{f}$ and $\mathbf{R}_\mathbf{n}$, which are called the power spectra of signal and noise, respectively. We thus can write:

$$\mathbf{R}_f = \mathbf{EAE}^{-1} \text{ and } \mathbf{R}_n = \mathbf{EBE}^{-1} \tag{2.22}$$

We can easily get the transpose of **H** from Eq. (2. 7), given by:

$$\mathbf{H}^T = \mathbf{ED}^*\mathbf{E}^{-1} \tag{2.23}$$

where D* is the complex conjugate of the matrix **D**. Choosing matrix **Q** such that $\mathbf{Q}^T\mathbf{Q} = \mathbf{R}_f^{-1}\mathbf{R}_n$, using Eqs. (2.7), (2.22) and (2.23), and multiplying Eq. 2.19 by $\mathbf{E}^{-1}$, after some matrix manipulations we have:

$$\mathbf{E}^{-1}\hat{\mathbf{f}} = \left(\mathbf{D}^*\mathbf{D} + \gamma\mathbf{A}^{-1}\mathbf{B}\right)^{-1}\mathbf{D}^*\mathbf{E}^{-1}\mathbf{g} \tag{2.24}$$

where the elements of **A** and **B** are the Fourier transforms of the elements in $\mathbf{R}_f$ and $\mathbf{R}_n$, respectively. As we have mentioned, these terms are the power spectra of signal and noise and will be denoted by $P_f(u,v)$ and $P_n(u,v)$, respectively.

Choosing $\gamma = 1$, we get the following equation in the frequency domain:

$$\begin{aligned}\hat{F}(u,v) &= \left[\frac{H^*(u,v)}{|H(u,v)|^2 + P_n(u,v)/P_f(u,v)}\right]G(u,v) \\ &= \left[\frac{1}{H(u,v)}\frac{|H(u,v)|^2}{|H(u,v)|^2 + P_n(u,v)/P_f(u,v)}\right]G(u,v) = H_W(u,v)G(u,v)\end{aligned} \tag{2.25}$$

for u and $v = 0, 1, \ldots, M\text{-}1$ ($M = N$). The Wiener filter is given by the term within bracket:

$$H_w(u,v) = \frac{1}{H(u,v)}\frac{|H(u,v)|^2}{|H(u,v)|^2 + P_n(u,v)/P_f(u,v)} \tag{2.26}$$

From the above equation, we can see that the Wiener filter consists of two parts, the inverse filter and the Wiener estimator as shown in Fig. 11.

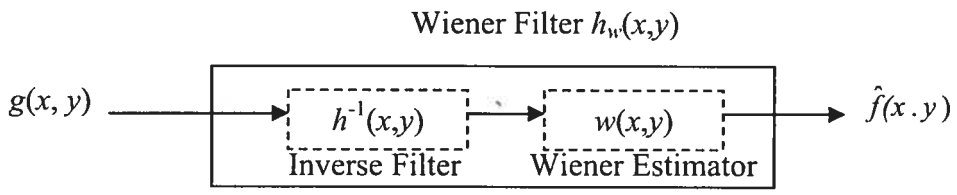

Figure 11: The block diagram of the Wiener filter.

It is noted that the derivation of the Wiener filter is based on a statistical model of the image in which the measured image is a single realization of a random field. The result obtained by using the Wiener filter is thus optimal in an average sense.

Equation (2.26) can be easily extended to three dimensions:

$$H_w(u,v,w) = \frac{H^*(u,v,w)}{|H(u,v,w)|^2 + P_n(u,v,w)/P_f(u,v,w)} \tag{2.27}$$

Hence, using the Wiener filter, one can estimate the original image under the assumption that we have *a priori* information such as the PSF of the imaging system and the power spectra of the original image and noise are known.

2.4 Adaptive Wiener filter

2.4.1 Limitations of the Wiener filter

The needed conditions to apply the Wiener filter is that the PSF of the imaging system and the power spectra of the signal and the noise are known. However, this is not the case in practical use. In this work, therefore, we propose an adaptive Wiener filter that uses a reference image as the original image and estimates the PSF and the power spectra of noise according to an image contrast-mottle criterion.

Metabolic SPECT and anatomic MRI brain images contain complementary information necessary to interpret brain function and pathology. SPECT images can offer physiologic information such as cerebral blood flow, cerebral oxygen utilization, local glucose metabolism and local protein synthesis, but with lower spatial resolution, while MRI scans provide good soft tissue discrimination and higher spatial resolution. In clinical application, patients often receive both MRI and SPECT scans.

Firstly, we propose using the MRI scan as a reference image (after a set of processing) for providing *a priori* information about the non-degraded SPECT image.

Secondly, we make an assumption that the PSF of SPECT imaging system is a Gaussian function with an unknown variance. In addition, it is assumed that the additive noise introduced by the system is an AWGN. Although this assumption is only an approximation of the reality, it is widely used in the literatures and we will show later that it is acceptable to improve the SPECT images.

Lastly, with the contrast-mottle criterion, the adaptive Wiener filter can iteratively estimate the parameter of the PSF and the power spectrum of the noise to finally restore the SPECT image.

2.4.2 Image contrast-mottle criterion

In Nuclear Medicine, subject contrast comes from the ability of the agent to be selectively taken up by the organ of interest and by the timing of imaging processing to coincide with the maximum uptake of the radiopharmaceutical. In the context of biomedical engineering, the increase of the dose of the radiopharmaceutical is strictly forbidden, and increasing data acquisition time can introduce movement of organs, therefore the contrast of SPECT images is hard to be improved.

However, the contrast of an image is very important for diagnosis. To visualize a given lesion, the contrast should be high enough to overcome the loss of visibility due to the presence of noise. For this reason, we introduce the image contrast-mottle criterion [WLOLF85] [MM00], into our restoration procedure to choose the best combination of two parameters for the adaptive Wiener filter so that the recovered image contrast is enhanced while the amplification of mottle is acceptable.

If $f(x, y)$ represents the intensity of a pixel located at the position (x, y), the image contrast can be defined in the following ways [Mig03]:

* Standard deviation of gray levels in the image

$$C = \sqrt{\frac{1}{MN}\sum_{x=0}^{N-1}\sum_{y=0}^{M-1}(f(x,y)-m)^2} \tag{2.28}$$

where m is the average intensity of the image.

* Variation between maximum and minimum intensity values in the image.

$$C = \frac{\max[f(x,y)] - \min[f(x,y)]}{\max[f(x,y)] + \min[f(x,y)]} \tag{2.29}$$

* Relative difference of intensity in the image

$$C = \left| \frac{m_A - m_B}{m_B} \right| \tag{2.30}$$

where m_A and m_B represent the mean values in the region A and B of the image, respectively.

In this work, the definition of the contrast is based on the third method. Brain SPECT images have three main regions of interest, Gray Matter (GM), White Matter (WM) and Cerebrospinal Fluid (CSF). The average contrast is defined between the WM and GM regions [MM00],

$$C = 1 - \frac{m_{WM}}{m_{GM}} \tag{2.31}$$

where m_{WM} and m_{GM} are the mean values of the pixel intensity in the regions of white matter and gray matter respectively, C represents the average contrast.

The mottle is characterized by taking the ratio of the standard deviation of pixel value to the mean in one region and defined by Mignotte *et al.* [MM00] as:

$$M_{WM} = \frac{\sigma_{WM}}{m_{WM}} \text{ and } M_{GM} = \frac{\sigma_{GM}}{m_{GM}} \tag{2.32}$$

where σ_{WM} and σ_{GM} are the standard deviation of the pixel intensity in the areas of WM and GM respectively. The average mottle of the image is thus defined by:

$$M = \rho_{WM} M_{WM} + \rho_{GM} M_{GM} \tag{2.33}$$

where ρ_{WM} is the proportion of pixels belonging to the area of white matter and the same meaning for ρ_{GM}.

The above average contrast and mottle criteria are used to evaluate the performance of image restoration techniques in [WLOLF85] [MM00]. The contrast is

the parameter that we intend to increase so that the image can be enhanced by means of restoration technique. The mottle parameter is used to measure the amplification of noise and/or the presence of artificial effects that are the side effect generated by restoration processing. It is the parameter that we want to control.

In order to increase image contrast, we introduce this contrast-mottle evaluation criterion into our restoration process. Two parameters will be adjusted such that the current mottle is under a threshold and the current contrast is maximum. If this criterion is met, the adaptive Wiener filter will choose this best combination of its parameters so that the recovered image contrast can be maximally increased while its noise amplification and the artifacts are under acceptable level.

2.4.3 The formulation of the adaptive Wiener filter

The adaptive Wiener filter consists of two major tasks, estimating the parameter of the PSF and the power spectrum of the noise.

As for the estimation of the PSF, it is generally implemented in two steps. The first step is making assumptions on the characteristics of the PSF. A popular method is using parametric models such as 1D uniform local averaging of neighboring pixels for linear motion blur, uniform intensity distribution within a circular dist for out-of-focus blur, Gaussian function for atmospheric turbulence blur and other imaging blur. The PSF parameters are then characterized by the features of the true and blurred images. For example, for astronomical speckle imaging, the PSF can be identified by a point source against a uniform background [Bat82]. In the frequency domain, zeros are resulting from situations in which the source of blurring is linear motion [Can76] [CTE91][Cha91][FM91].

In section 1.2 we described the degradation sources of SPECT imaging and modeled the blurring effect as a Gaussian function PSF with zero mean. The estimation of the SPECT PSF thus becomes only estimating the standard deviation of the Gaussian function (assumed isotropic) or the PSF width (σ).

Rooms *et al.* proposed a wavelet based method that measures the sharpness of edges in the blurred image by calculating the magnitude of the Lipschitz exponent and

finds out the relation between this value and the standard deviation of Gaussian PSF [RRPP02]. However this technique is noise sensitive.

In section 2.4.1, we mentioned that the parameter of the Gaussian PSF and the power spectrum of noise would be estimated iteratively according the contrast-mottle criterion. The detailed iteration process will be explained in section 4.1.3. Experiments will show that our method has a good tolerance to noise, in other words, the identification of PSF can be estimated under noisy situation.

Now let us discuss the estimation of the term P_n/P_f in Equation (2.28). This term can be interpreted as the reciprocal of the signal-to-noise ratio. In conventional ways, the power spectrum of the true image P_f is approximated by one of the observed image. This obviously is a quite rough estimation. Gonzalez and Wintz proposed using a constant in proportion to the standard deviation of the noise term to replace the P_n/P_f in [GW87]. This method is simple but still needs the knowledge of noise. In this work, since we introduce a reference image that is very close to the true scene, P_f is obtained by calculating the power spectral density of this reference image (MRI) after an appropriate gray level assignment (see section 3.3.4).

As the noise term is modeled as AWGN, its power spectral function does not vary with frequencies and is equal to its variance everywhere. Hence, the 3D adaptive Wiener filter can be formulated by

$$H_{AW}(u,v,w,\sigma,K) = \frac{H^*(u,v,w,\sigma)}{\left|H(u,v,w,\sigma)\right|^2 + K / P_f(u,v,w)} \tag{2.34}$$

where $H(u,v,w,\sigma)$ represents the three dimensional Fourier transform of the Gaussian PSF with unknown standard deviation σ. $H^*(u,v,w,\sigma)$ is the complex conjugate of $H(u,v,w,\sigma)$. K denotes the constant power spectrum of the AWGN that we have to estimate.

Fig. 12 shows the functional diagram of our adaptive Wiener filter. The whole process needs two inputs, one is the raw SPECT image and another is the raw MRI volume. The reference image is obtained by preprocessing (e.g. registering) the raw MRI volume with respect to the raw SPECT volume image.

It is easy to find that the adaptive Wiener filter is a non linear restoration method due to the introduction of the contrast-mottle criterion. The iterative results converge when the combination of the two parameters, the PSF width (σ) and the constant power spectrum of noise (K), makes the restored image meet the contrast-mottle criterion.

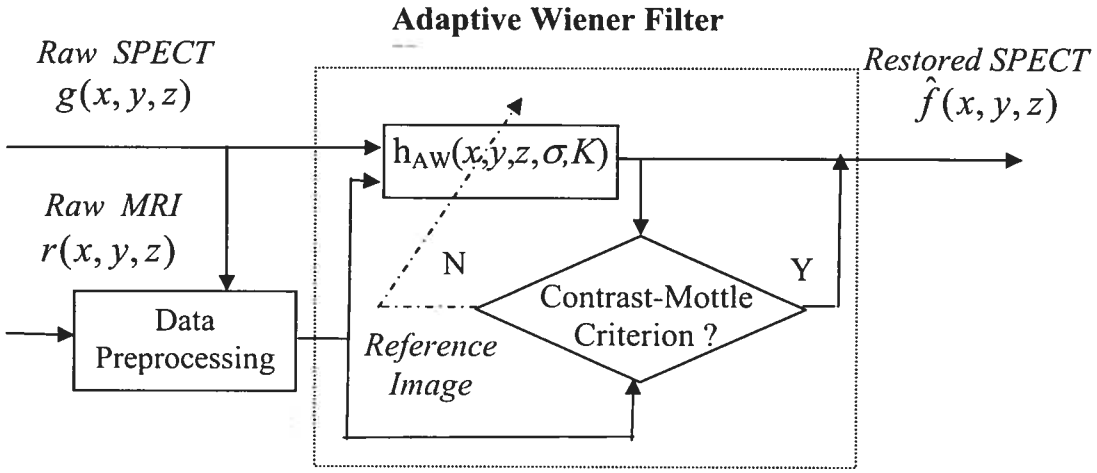

Figure 12: Interpretation of the proposed technique.

Chapter 3

MRI Data Preprocessing

3.1 Introduction

Adaptive filters are these filters that are capable of self adjustment. The adaptive Wiener filter requires two inputs: the degraded image to be processed and the reference image. However, the original MRI volume can not be directly employed as the reference image. We have to apply a number of image processing techniques to make the original MRI data become the reference image. Figure 13 summarizes the major tasks for the whole system including a 4-step data preprocessing (during which only the MRI data is processed) and the iterative restoration procedure that we defined in section 2.4.3. The data preprocessing consists of (1) removing skull, scalp and other non brain material from the raw MRI volume, (2) registering the previous image with regard to the SPECT image, (3) segmenting the registered brain MRI volume into three brain regions (GM, WM and CSF), and (4) assigning regional cerebral (SPECT) activity for GM, WM and CSF regions in the previous result.

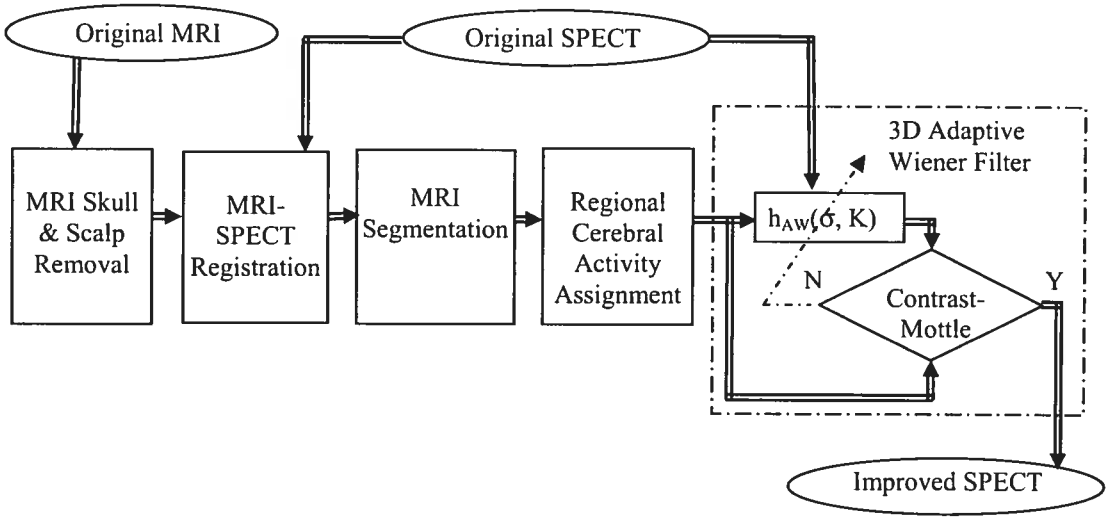

Figure 13: The block diagram of the system.

We received raw MRI and SPECT images from the CHUM (University of Montreal Medical Center). The original data is stored in DICOM format (section 1.4 gives the description of this standard). Since MRI and SPECT images come from two different and complementary imaging modalities, they have different voxel sizes, and different intensity values for the three main brain regions. It is evident that the original MRI scan could not meet the requirement as a reference image without being processed. Fortunately, in digital image processing, segmentation and registration techniques can help us to achieve this goal. A short introduction about image segmentation and registration will be presented in section 3.2. Section 3.3 contains the detailed description of each data preprocessing technique.

3.2 Segmentation and registration

Segmentation and registration are two of the most important image processing techniques. We will address these two issues in the following subsections.

3.2.1 Segmentation

Segmentation is to partition an image into several constituent components, in other words, to classify each image pixel to one of the image parts. The purpose of segmentation is usually to extract areas of interest from an image for subsequent processing. Although a variety of techniques exist to segment an image, the principles of these methods are generally based on one of two basic properties of gray-level values: discontinuity and similarity [GW87].

In the first class, the detection of discontinuity is based on sudden changes in gray level. The approaches among this category detect isolated points, lines, and edges in an image through small spatial masks.

However, when noise and other effects that introduce artificial intensity discontinuity are present, these masks alone are not sufficient. They are typically

followed by further local or global analysis to link edge pixels into a meaningful set of object boundaries.

In the second class, thresholding and region growing are two common segmentation approaches using the property of gray-level-value similarity.

Thresholding is one of the most important approaches for image segmentation. Techniques in this group are on a basis of pixel gray values. One way to choose thresholds is via an image histogram. In many situations, histograms are composed of several regions, so one can select those gray values lying on boundaries as thresholds, by which the images are segmented. Thresholding is also the most basic segmentation method, often followed by or combined with other methods, such as optimal procedure, boundary characteristics, multiple variables to characterize each pixel, and models used to deal with more complicated gray-level-value situations. The technique we used for the MRI brain/non-brain segmentation is a thresholding method with a surface model. We will describe it in section 3.3.1.

Region-growing segmentation, as implied by its name, is accomplished via connecting pixels and small regions into larger regions. The methods start by selecting a set of seed points inside each regions, from which regions are grew by adding their neighborhood that have similar properties, such as same gray range, or same texture, etc. We shall use this technique for our data processing. A more detailed description will be given in section 3.3.3.

3.2.2 Registration

Registration is a critical stage for comparing and visualizing different images. Indeed, for providing *a priori* information, the MRI data should be aligned with the SPECT image. Performing registration is therefore a necessary step to achieve this goal. The registration is defined as a technique that determines the spatial alignment between images of the same or different subjects, acquired with the same or different modalities [Der01].

There are a wide variety of registration methods. Maintz and Viergever classified medical registration methods based on nine basic criteria as follows [MV98],

* Dimensionality: spatial dimensions only or time series with spatial dimensions.
* Nature of registration basis: extrinsic, intrinsic and non-image based
* Nature of transformation: rigid, affine, projective and non-linear
* Domain of transformation: local and global
* Interaction: interactive, semi-automatic, and automatic
* Optimization procedure: parameters computed and parameter searched for
* Modalities involved: mono-modal (intra-modality), multi-modal (inter-modality), modality to model, and patient to modality
* Subject: intra-subject, inter-subject, and atlas
* Object: head (brain), thorax, abdomen, etc.

It is noted that a particular registration algorithm can possess different criteria at the same time.

Based on these criteria, the registration method chosen for our work is a 3D, brain, intra-subject, inter-modality, automatic, global and linear registration.

During the process of registration, a transformation or mapping between the coordinates in one space and those in another has to be determined so that biological, anatomical or functional correspondence can be achieved.

There are different types of transformation. Each type depends on the assumption made for the medical images to be registered. If the structures of interest in the images are either bone or enclosed in bone, such as brain, rigid body transformation will be used, where individual bones are considered as rigid at the resolution of radiological imaging modalities. This rigid body transformation has six degrees of freedom or unknown including three translations and three rotations.

When tissues deform in more complicated ways involving, for example, scaling or skewness or sharing resulting from different imaging systems, an affine transformation is useful for overcoming these problems. An affine transformation has 12 degrees of freedom. We can naturally consider a rigid transformation as a special case of affine, in which the scaling values are all unity and the skewness and sharing are zero.

If we want to align images more accurately, even for the brain, in the case of development of children, lesion growth, or different subjects, additional degrees of freedom are needed. In this type of application, an affine transformation is first used to give an approximate alignment, higher degree of freedom or non-linear registration algorithms are then implemented.

In literature a number of methods have been reported to determine a registration transformation. Many researchers use geometric features for rigid body registration. Point-based methods, for example, use singular value decomposition techniques [EBMTH88] [HHCGCBSG91] to resolve the Procrustes problem to finally determine this transformation. Surface matching method, such as the head-and-hat algorithm, takes advantage of high-contrast skin surface–the boundary between tissue and air–to measure the distance between a point on the hat (the image to be registered) and the nearest point on the head (the higher-resolution image) [LPCC88], using the Powell iterative optimization technique [PTVF92] to get the final solution.

Other researchers use voxel similarity measures. One of the simplest methods is to minimize the sum of square intensity differences (SSD) between two images based on the assumption that the images differ only by Gaussian noise after registration. Correlation techniques suppose that the intensity values in two images possess a linear relationship, in which the correlation coefficient is optimized. These methods are usually applied for intra-modality registration. As for inter-modality registration, the situation becomes more complex. The method proposed by Woods *et al.* [WMC93] is originally for MRI-PET registration. It is the first widely used inter-modality registration algorithm by measuring voxel intensity similarity. The software package AIR (Automated Image Registration) [AIR02] is created by Woods *et al.* to supply brain inter-modality registrations. We will present this algorithm later (section 3.3.2) and use it for our MRI-SPECT registration.

3.3 MRI data preprocessing

The MRI data was acquired by a SIEMENS system. It is a sagittal T1-weighted MRI consisting of a series of 144 planes, with 512×512 pixels each. Voxel size is 0.5 mm in plane, with slice thickness of 1 mm.

3.3.1 Removal of skull and scalp with Brain Extraction Tool (BET)

Because the brain MRI data include skull, scalp, eyeballs, skin, fat, muscle, etc, while the brain SPECT image does not, we need to exclude these non brain structures from the raw MRI scan so that the registration, which is the necessary step for the raw MRI scan to become the reference image, can be made more accurately.

The techniques to remove the skull and scalp while maintain the brain including only GM, WM, and CSF are called "stripping", "skull-stripping", "brain/non-brain segmentation", or "brain extraction". Brain extraction algorithms fall into the category of image segmentation.

There are three major brain extraction algorithms: manual, threshold-with-morphology and surface-model-based [Smi02]. The Brain Extraction Tool proposed by Smith [Smi02] is the third one, which is selected for our MRI brain/non-brain segmentation.

Smith defines a surface model with a tessellated mesh of triangles shown in Fig. 14, and then uses two constraints, one that imposed some form of smoothness on the surface and another that fitted the surface model to the brain surface, to find an optimal solution iteratively.

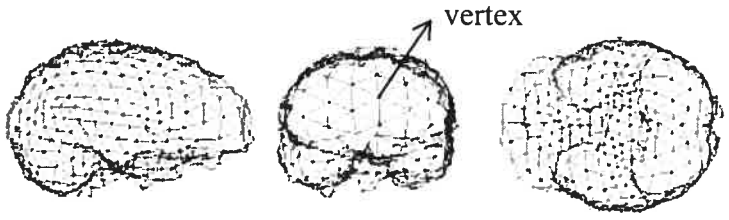

Figure 14: Three views of a surface mesh.

The method starts with calculating the intensity histogram of a 3D brain image. The intensity minimum t_2 (2% of voxel intensities below this value) and maximum t_{98} (2% of voxel intensities over this value) thresholds are then found from the histogram. A

rough brain/background threshold t is set to lie at 10% of the interval $[t_2, t_{98}]$. The centre of gravity (COG) of the brain/head is estimated by using all voxel intensities greater than t in a standard weighted sum of position. The mean "radius" r of the brain/head is also roughly estimated by accounting all voxels with intensity greater than t.

After that, the spherical tessellated surface is initially centered on the COG with its radius set to half of the estimated value r, and then the main iterated loop is executed. At each iteration, an update of each vertex in the tessellated surface is performed by estimating where that vertex should move to for improving the surface. To find an optimal solution, the BET uses a small movement update (small relative to the mean distance between neighboring vertices) with many iterations (typically 1000). For each vertex, the small movement update vector **u** is calculated from three terms: within-surface vertex spacing, surface smoothness control, and brain surface selection term. The third term is parallel to the normal of a difference vector that takes the current vertex to the mean position of its neighbors (if this vector were minimized for all vertices, the surface would be forced to be smooth and all vertices would be equally spaced). This term is actually interacts with the image and attempts to force the surface model to fit to the real brain surface.

The final brain surface model is found by performing a check for self-intersection. To save computation time, the vector **u** in the main loop does not taken into account this check. If the surface is self-intersected, the main iterated loop is re-run with much higher smoothness constraint for the first 75% iterations and linearly dropped down to the original level for the rest of iterations.

The major procedures of BET are illustrated by Fig. 15 and its implementation can be found in the MRIcro software package.

3.3.2 MRI-SPECT registration with AIR

Since we do not focus on image registration in this work, the MRI-SPECT registration problem will be dealt with by an automated tool. The AIR package supplied by Woods *et al.* satisfies our requirement for brain intra-subject and inter-modality registration.

Woods *et al.* proposed an automated inter-modality registration algorithm in 1993 [WMC93], in which the MRI-PET registration problem was addressed. This algorithm is a voxel-intensity-similarity method. The AIR software package is developed based on this algorithm and offers many linear and non linear methods for 3D inter-modality registration. Each of these methods has its own model. Here we only mention one model applied for our application, affine 12-parameter model, which is a linear transformation plus translation and defined by:

$$\begin{bmatrix} x' \\ y' \\ z' \\ 1 \end{bmatrix} = \begin{bmatrix} a & b & c & d \\ e & f & g & h \\ i & j & k & m \\ 0 & 0 & 0 & 1 \end{bmatrix} \begin{bmatrix} x \\ y \\ z \\ 1 \end{bmatrix} \tag{3.1}$$

where $[x', y', z']$ and $[x, y, z]$ are the coordinates of MRI and SPECT respectively.

The transformation parameters for inter-modalities registration in AIR are calculated by minimizing a criterion $\tau = \sum_j \omega_j \times n_j / N$ with $\omega_j = \sigma_j / m_j$ and $N = \sum_j n_j$, where the parameters are described as follows: τ is the weighted average of the normalized standard deviations measured for the variations MRI voxel values. For any voxel position i whose intensity is j in the MRI study, there is a corresponding SPECT voxel whose intensity value is α_{ij}. Let σ_j and m_j represent the standard deviation and the mean of α_{ij} respectively for all voxels n_j, which is the total number of voxels whose intensity is j within the brain in the MRI study. It is assumed that τ is minimum when two volumes are registered. The optimization algorithm is the Newton-Raphson method.

Once the transformation matrix (Eq. 3.1) is computed, a mapping from the old coordinate to the new one for each point of the MRI data is then performed. For the execution of this mapping, we need to interpolate intensity values because most points do not fall on the volume discrete grid (voxel). Trilinear interpolation is sufficiently accurate for our application and is defined by:

$$\begin{aligned} I_{xyz} &= I_{000}(1-x)(1-y)(1-z) + I_{100}x(1-y)(1-z) + I_{010}(1-x)y(1-z) \\ &+ I_{001}(1-x)(1-y)z + I_{101}x(1-y)z + I_{011}(1-x)yz + I_{110}xy(1-z) + I_{111}xyz \end{aligned} \tag{3.2}$$

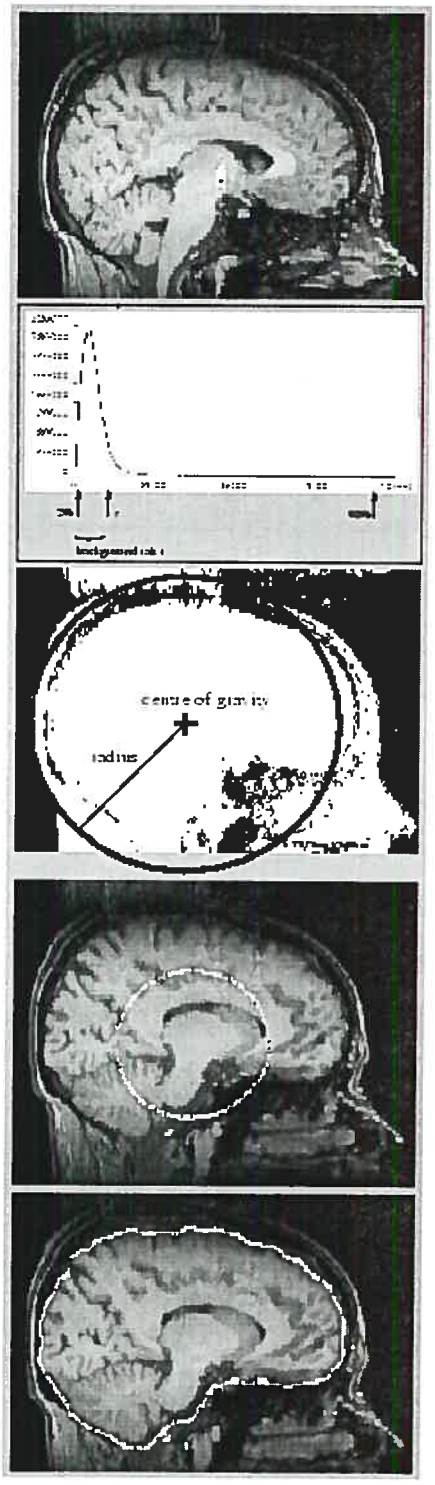

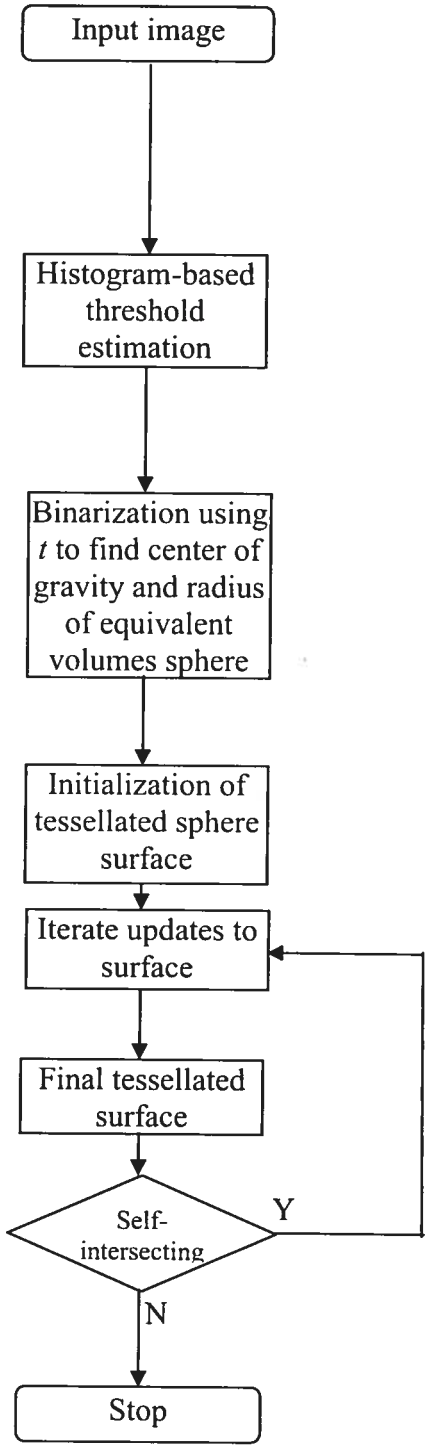

Figure 15: The flow chart of the Brain Extraction Tool.

where I represents the intensity at each point. Figure 16 explains the relationship between a point (x, y, z) that is not on the discrete grid and its 8-voxel neighborhood.

It is noted that in order to have a better performance of registration, we manually implement a rescaling and a roughly centering process on MRI data prior to the affine transformation.

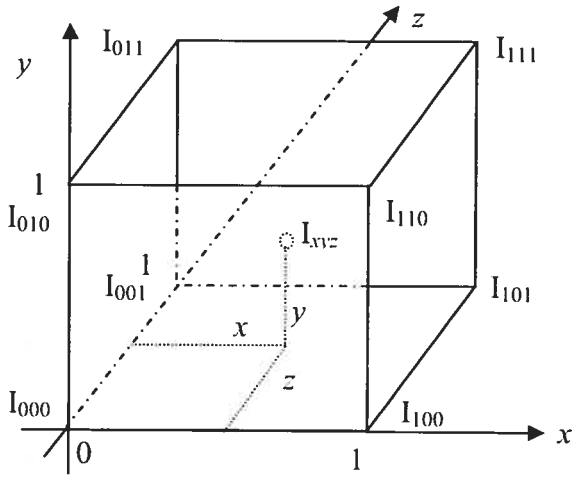

Figure 16: Trilinear interpolation.

3.3.3 Segmentation of the registered MRI volume

After registration, the MRI volume has been aligned with the SPECT volume. The final purpose of using the MRI data is to provide a reference image that contains only three regions of brain, gray matter, white matter and Cerebral-Spinal Fluid. We use a region-growing segmentation method to achieve this goal.

Since region-growing is the most basic segmentation approach, the software toolkit ImageJ [IJ04] provides a method in this category, called connected threshold region growing. This method needs two inputs for extracting one particular region, a seed point and a growing criterion based on intensity similarity – two threshold values (high and low) for this region. The region grows from the seed point by checking its 6-

voxel neighborhood to verify if any meet the intensity threshold requirement. If they have intensity between the high and low threshold values, the method continues to grow from them as well. Other much more sophisticated algorithms, such as the one in [HCJD], exist for segmentation but are not necessary here.

With this region-growing segmentation method, we finally obtain a registered and segmented reference image that consists of only three regions of brain.

3.3.4 Regional cerebral activity assignment

Finally in the last step, each segmented region received an activity level (gray level value) corresponding to the expected SPECT activity of the radiotracer. This value may vary depending on the agent used for SPECT imaging [AM99]. In our experiments, we use Tc99m-ECD radiotracer and set the activity ratio between gray matter and white matter to 4:1.

Chapter 4

Experiment and Results

4.1 Restoration of synthetic brain SPECT image of Hoffman Phantom

4.1.1 Hoffman phantom

The 3D Hoffman phantom was developed by Hoffman *et al.* in 1990 [HCDM90]. This phantom contains three regions of the brain: gray matter, white matter and ventricle. The digital Hoffman phantom [DSC03] has the activity ratio of 4:1:0 for normal gray matter : white matter : ventricle (each voxel with intensity values from 0 to 255). We have mentioned early that this ratio may vary depending on the agent used for SPECT imaging, for example, using Tc99m-ECD produces 4:1 gray-to-white matter ratio while using Tc99m-HMPAO produces only 2.5:1 gray-to-white matter ratio [AM99]. The volume has 19 slices in axial plane with 128×128 pixels for each. The voxel size is 1.69mm×1.69mm×3.38mm. A slice of this phantom is shown in Fig. 17(a), in which an artificial hypoperfusion is added at the center of the small circle.

With the Hoffman phantom, *a priori* information is exactly known, so we can fully analyze the restored image resulting from the adaptive Wiener filter.

4.1.2 Synthetic SPECT

To get a synthetic SPECT volume, we apply the linear degraded model on the Hoffman phantom. You may recall that this model is defined by Equation (2.2): $\mathbf{g} = \mathbf{Hf} + \mathbf{n}$

Two synthetic SPECT volumes are created with two different pairs of parameters (the PSF width σ, and the variance of the Gaussian noise), which are (σ =2 voxels or 7.94 mm FWHM, 1000) and (σ = 3 voxels or 11.91 mm FWHM, 100), respectively,

noted $FWHM(mm) = \sigma(mm) \times 2\sqrt{2\ln 2}$. A slice of each synthetic SPECT volume is shown in figures 17(b.1) and 17(b.2). The corresponding degraded contrast and mottle values are (C_d = 18.10%, M_d = 32.70%), and (C_d = 7.80%, M_d = 24.91%). Notice that in a realistic situation, there should be no (Poisson) noise in the background, but because we use a simpler additive model for creating mottle.

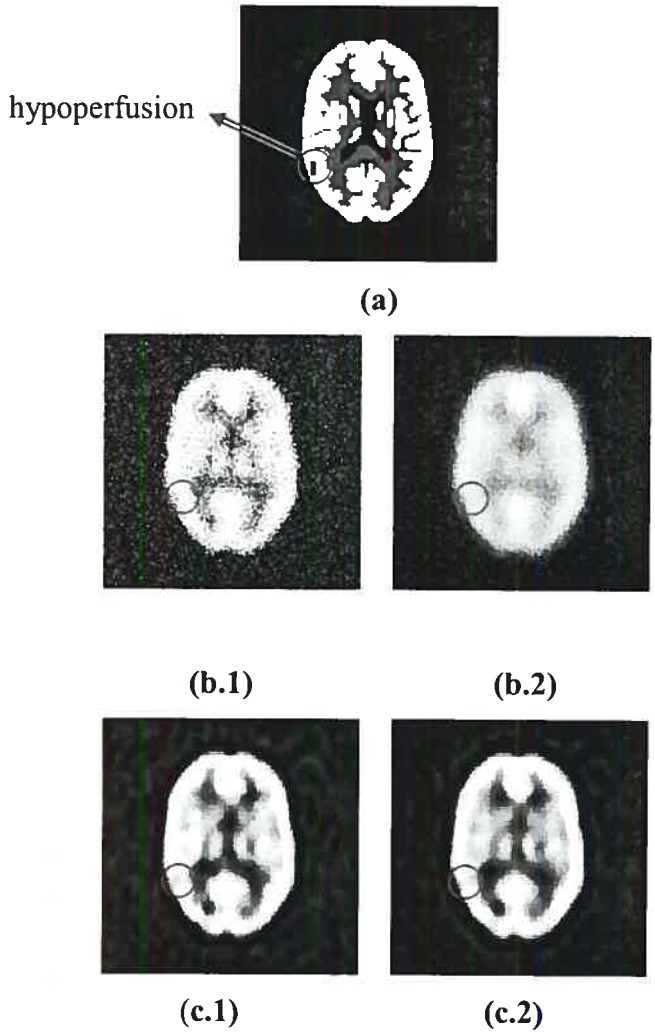

Figure 17: (a) Original Hoffman phantom slice. (b.1) Synthetic SPECT slice with PSF FWHM =7.94 mm and noise variance = 1000, contrast C_d =18.10% and mottle M_d =32.70% . (c.1) Restored image for (b.1), contrast C_r = 32.05% and mottle M_r = 27.75%. (b.2) Synthetic SPECT slice with PSF FWHM = 11.91 mm and noise variance = 100, contrast C_d =7.80% and mottle M_d =24.91% . (c.2) Restored image for (b.2), contrast C_r = 28.74 % and mottle M_r = 27.78%.

4.1.3 Restoration of synthetic brain SPECT image

For convenience, the adaptive Wiener filter formulation is listed below again

$$H_{AW}(u,v,w,\sigma,K) = \frac{H^*(u,v,w,\sigma)}{\left|H(u,v,w,\sigma)\right|^2 + K / P_f(u,v,w)} \tag{4.1}$$

where $H(u, v, w, \sigma)$ is the 3D FFT of $h(x, y, z, \sigma)$, which is a radial symmetry 3D Gaussian function centered at the origin with a standard deviation σ to be estimated:

$$h(x,y,z,\sigma) = A\exp(-\frac{x^2+y^2+z^2}{2\sigma^2}) \tag{4.2}$$

in which A is a normalization constant. The parameter K in Equation (4.1) is the constant power spectrum of noise that we have to estimate too.

The restoration process starts by an initialization routine and is followed by a tow-level nested loop (see Fig. 18).

Initialization:

0. Set $n = 0$, $\sigma = 1$ (not necessary be integer value) voxel (FWHM = 3.97 mm), the iteration step K_{step} be a value (e.g. 5, or 10), and the mottle amplification factor margin f_{margin} be a value (e.g. 1.2 or 1.4).
1. Calculate the mottle M^0 and contrast C^0 for the degraded image $g(x, y, z)$.
2. Set $K = 10^5$ and $C^0_{\max} = C^0$.

Two-level nested loop:

3. Calculate the adaptive Wiener filter $H_{AW}(u,v,w,\sigma,K)$ using the following equation with the initial values of the PSF width σ and the constant power spectrum of noise K:

$$H_{AW}(u,v,w,\sigma,K) = \frac{H^*(u,v,w,\sigma)}{\left|H(u,v,w,\sigma)\right|^2 + K / P_f(u,v,w)} \tag{4.3}$$

4. Get the estimated function in the frequency domain with:

$$\hat{F}(u,v,w) = H_{AW}(u,v,w,\sigma,K)\cdot G(u,v,w) \tag{4.4}$$

Then compute the 3D inverse FFT to obtain $\hat{f}(x, y, z)$.

5. Compute the mottle M_n and contrast C_n values of the estimated image $\hat{f}(x, y, z)$.
6. If C_n is larger than C_{n-1} and M_n is smaller than $f_{margin} \times M_0$, the inner loop is repeated with $K = K/ K_{step}$. Keep the maximum value of C_n as $C^{\sigma}_{\max}$.
7. If the above conditions do not hold, but $C^{\sigma}_{\max}$ is larger than $C^{\sigma-1}_{\max}$, repeat the outer loop by increasing σ by 1 (as previous stated, it is not necessary to be an integer) voxel (FWHM 3.97 mm).
8. If all conditions do not hold, stop iteration.

With this algorithm we obtained a restored images with contrast and mottle of (C_r = 32.05%, M_r = 27.75%) and (C_r = 28.74%, M_r = 27.78%), respectively, shown in figures 17(c.1) and 17(c.2). The estimated PSF values are exactly the same as the degraded value, σ = 2 (7.94 mm FWHM) and σ = 3 (11.91 mm FWHM), and the estimates of the noise term are also very close to the ones we added, 781.25 and 97.65 respectively.

Other more complex optimization schemes may be used to get the best set of parameters, but with no real improvement of the final image results.

In Fig. 17 (c.1) or (c.2) one can observe a clear improvement of the image quality and a hypoperfusion within the circle that was not visible in the degraded images.

4.2 Restoration of real brain SPECT image

4.2.1 Reference image

Figures 19(a) and 19(b) show a slice of the MRI and SPECT volumes in axial view, respectively. The voxel sizes and dimensions of MRI and SPECT images are (1.00mm×0.50mm×0.50mm, 144×512×512) and (1.86mm×1.86mm×1.86mm, 128×128×97) respectively. The voxel intensities vary from 0 to 255 for both images (0 is black and 255 is white). To transform the original MRI data into an appropriate

reference image, a 4-step processing: brain extraction, linear registration, segmentation, and regional cerebral activity assignment has to be done.

From figures 19(a) and 19(b), we can find that a huge difference exists in appearance of MRI and SPECT images. In order to make an accurate registration on the MRI volume, brain/non-brain segmentation is necessary. Using the MRIcro package, the brain of the MRI scan is automatically separated from the skull and scalp.

We use the AIR package to align the MRI volume with respect to the SPECT volume. (1) The program *manualreslice* allows us to rescale and center the MRI volume manually. To execute this function, we only need to enter a desired voxel size (same as SPECT voxel size), new matrix dimensions (same as SPECT volume dimensions) and a translation value along z-axis (84 is chosen). The image produced by this program is shown in Fig. 20(b). (2) The program *alignlinear* implements 3D affine transformation. This program has several options. We choose a Gaussian filter with FWHM of 8mm×8mm×8mm along each dimension to smooth the brain-only rescaled MRI file. The option threshold, an integer value used to exclude low intensity, was set to 10 for both resliced and standard files (the MRI and SPECT intensities range from 0 to 255).

The program *reslice* takes the results of *alignlinear* to produce a realigned file. Figure 20 (c) shows the brain-only rescaled and registered MRI volume.

After registration, using the ImageJ toolkit with a Region Growing algorithm, we segment GM and WM into two files. The seed for GM or WM is easily chosen by selecting a point in each region. The low and high thresholds for GM and WM regions are manually chosen (here are {45, 72} and {71, 97}, respectively). We then combine these two binary images to one file, in which a voxel segmented into both GM and WM regions is assumed to be in the GM region.

Finally, using 4:1 for the activity ratio of gray matter and white matter, we set the GM gray level to 200 and the WM to 50. The results are shown in Fig. 20(d).

4.2.2 Restoration

After above four procedures, we are ready to do our real mission, to restore the brain SPECT image (Fig. 21(a)) with the help of the reference image (i.e. the registered

and segmented MRI volume). The restoration process has been described in Section 4.1.3. Here, a summary of this algorithm is given again in Fig. 18. The adaptive Wiener filter restores the SPECT volume with σ = 13.11 mm FWHM and K = 1562.5. The contrast and mottle in the images before and after the restoration are (4.46%, 19.82%) and (10.38%, 27.64%) respectively, see Fig. 21.

Table 1 summarizes all results, and figures 22-23 give the relationships between contrast/mottle and the estimated parameters. We will discuss them in the next section.

4.3 Discussion

You may recall that image restoration has conflicting goals, removing blurring and not creating noise at the same time. Obviously, this is an ideal solution but almost impossible to be realized. We have to take a balance between an image with more details and higher noise and an image with less sharpness but lower noise. We aim to deblur as much as possible while keeping amplification of noise under an acceptable level.

For the restoration of synthetic SPECT, two scenarios were realized. The case shown in Fig. 17(b.1) represents a relatively smaller blurring effect (FWHM is 7.9 mm), with a higher noise level (the noise variance is 1000). The image produced by the adaptive Wiener filter improves the image contrast by a factor of 1.77 (from 18.1% to 32.05%) while the mottle is even decreased to 84.8% of the original value (from 32.70% to 27.75%). This is because the adaptive Wiener filter performs just like the original Wiener filter and is capable to reduce noise if blurring is low. Figure 17(b.2) shows the situation where a heavier blurring (11.91 mm FWHM) is present but the noise level is a relatively lower (the noise variance is 100). The contrast in the recovered image, Fig. 17(c.2), has been dramatically increased to 28.74% from 7.8% (a factor of 3.68) but at the price of a little mottle amplification, a factor of 1.12 (from 24.91 to 27.64). The artificial hypoperfusion is clearly revealed in the restored images in figures 17(c.1) and 17(c.2) while there is no trace in the corresponding degraded images.

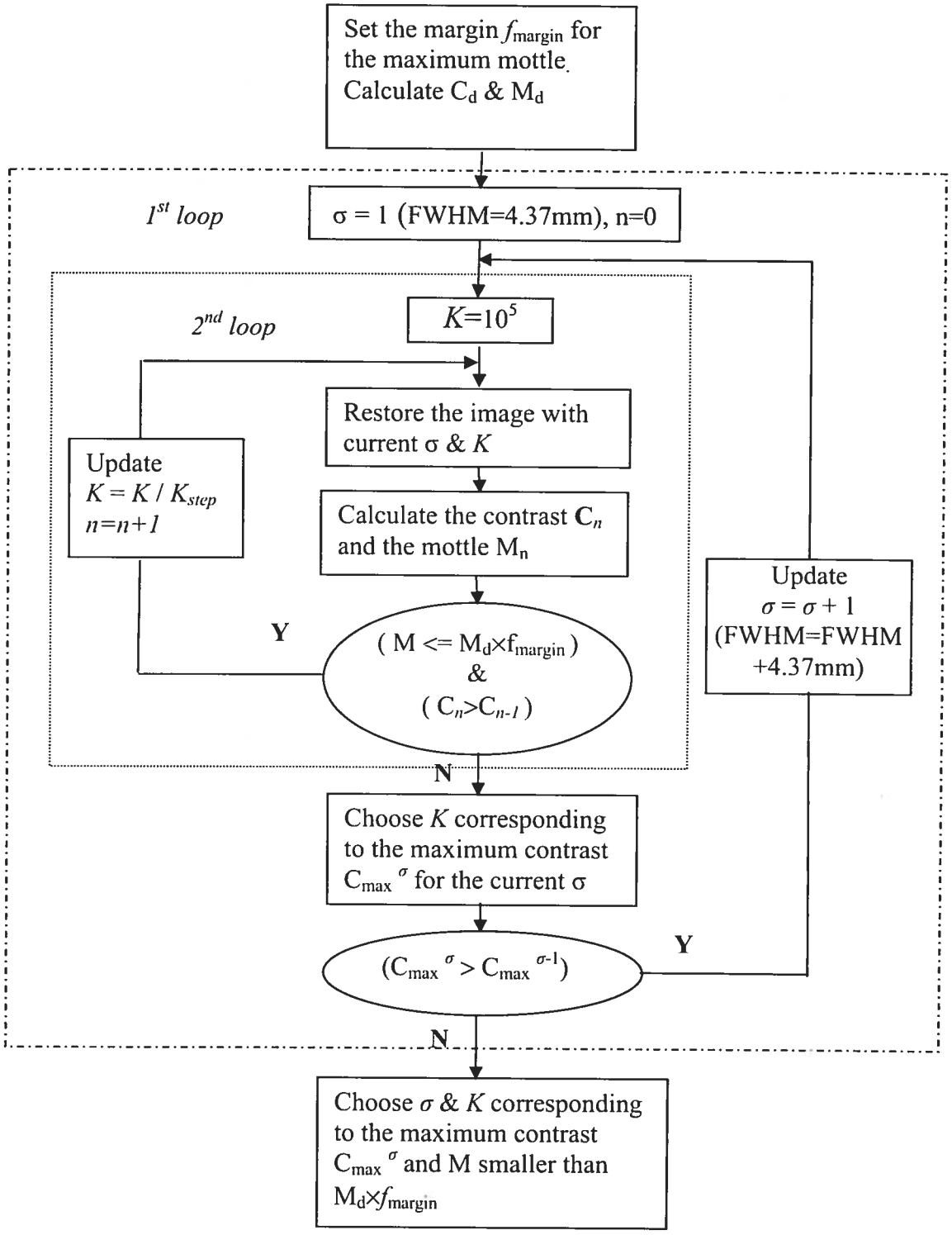

Figure 18: The flow chart of the adaptive Wiener filter.

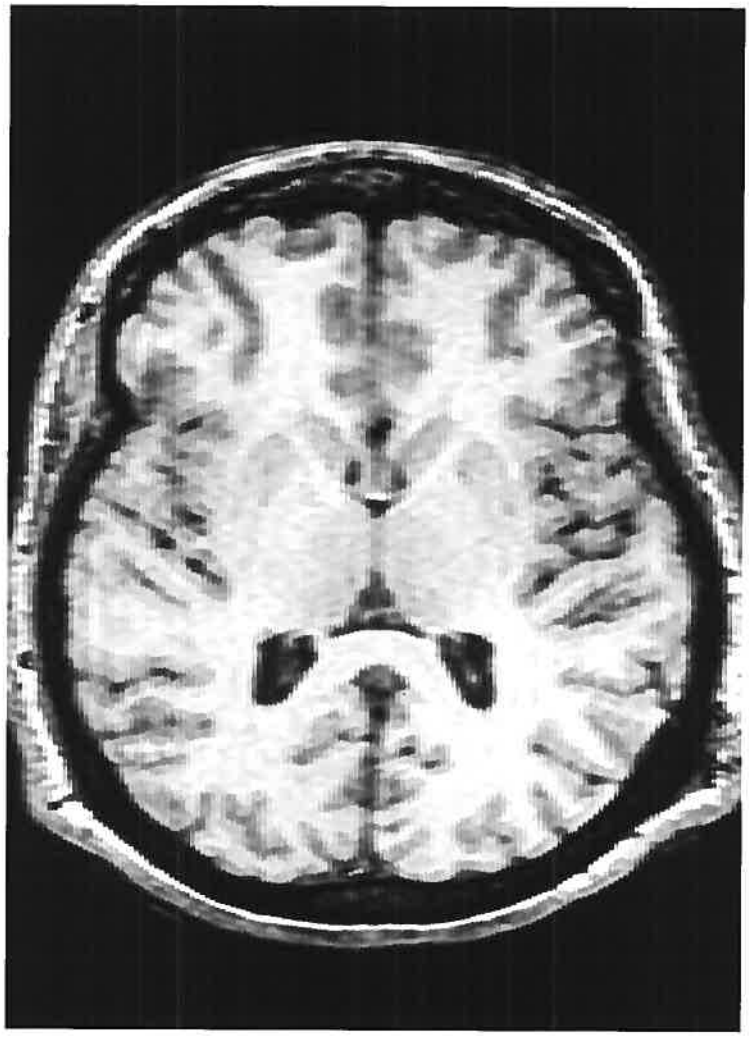

(a)

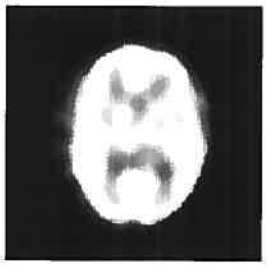

(b)

Figure 19: (a) A slice of the MRI volume in axial view. (b) A slice of SPECT volume in axial view.

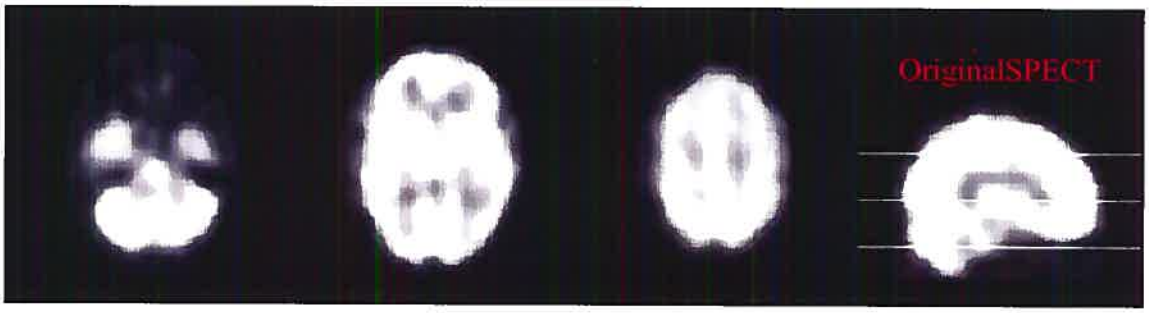

(a)

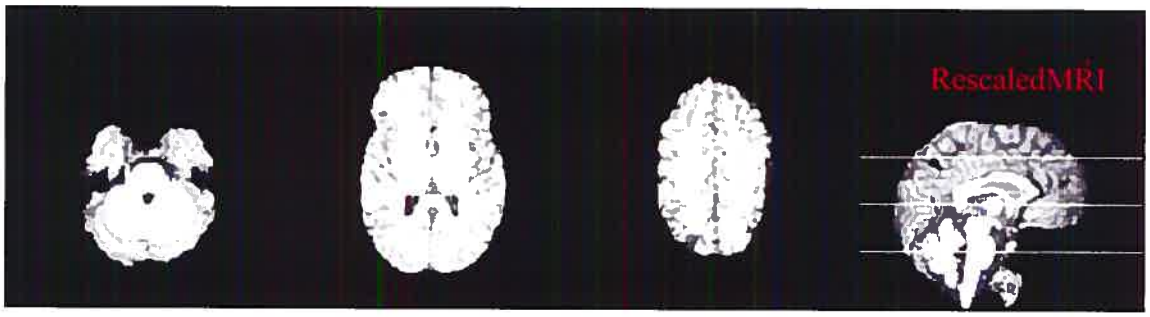

(b)

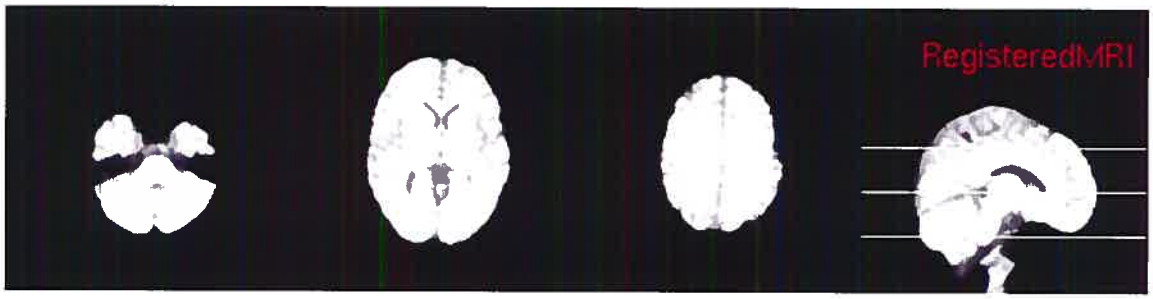

(c)

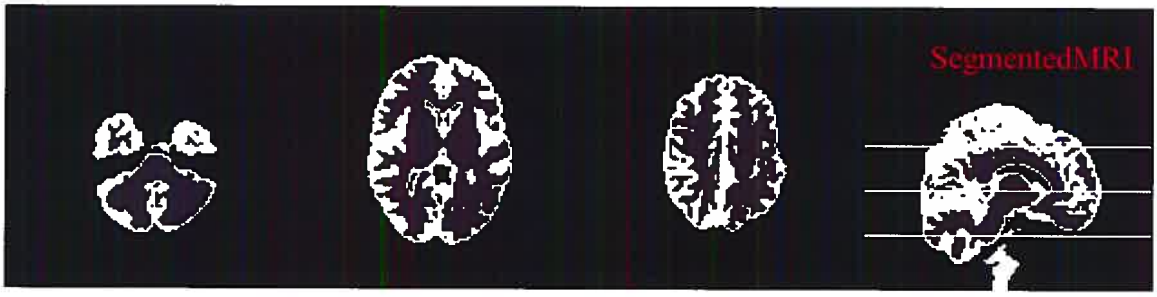

(d)

Figure 20: (a) The original SPECT. (b) The MRI after brain extraction and scaling. (c) The registered MRI. (d) The segmented and registered MRI.

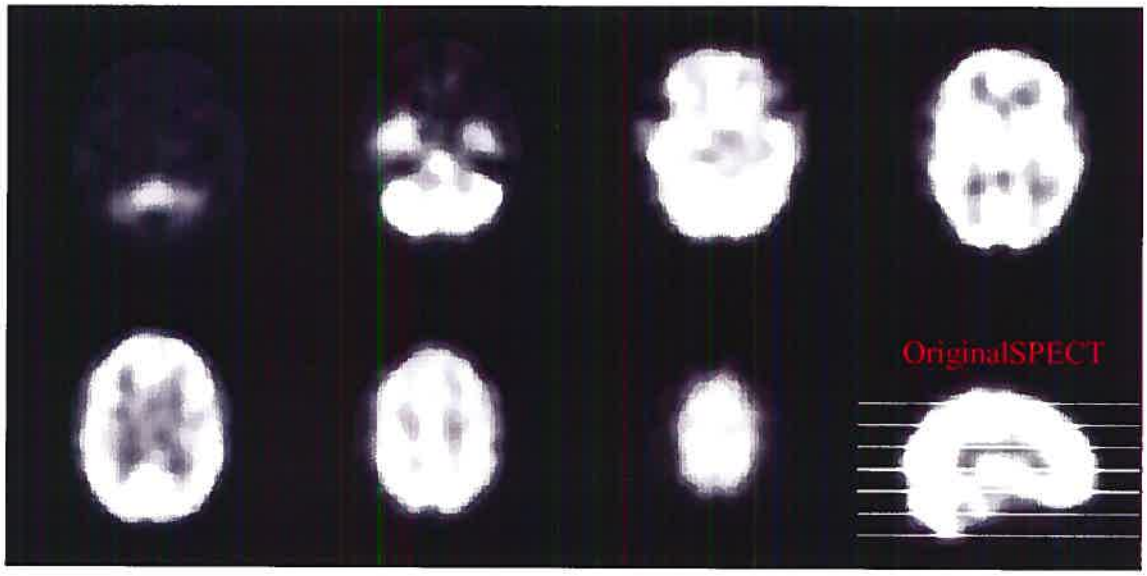

(a)

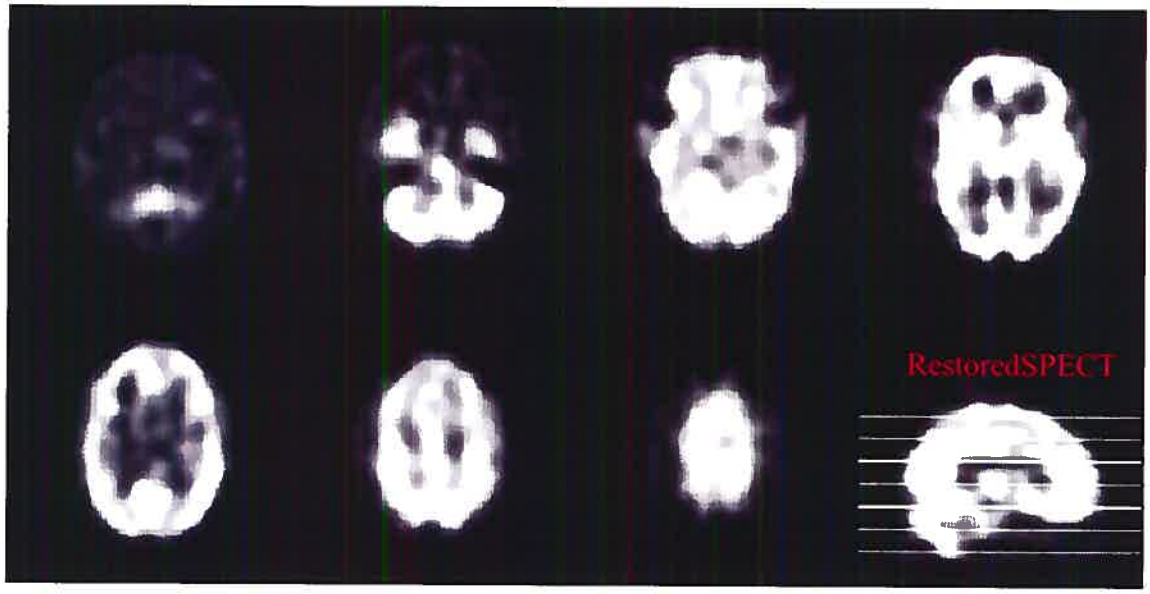

(b)

Figure 21: (a) The original SPECT image. (b) The restored SPECT image.

Studies	Degraded Image		Margin (f) for the Maximum Acceptable Mottle (M_{max})	Restored Image		
	Contrast %	Mottle %		Contrast % (factor)	Mottle %	Estimated Parameters
Synthetic SPECT #1 FWHM =7.94mm, σ_{noise}^2=1000	18.10	32.70	f= 0.85 M_{max}= 27.79	32.05 (f_c=1.77)	27.75	FWHM $_{est}$ =7.94mm K=781.25
Synthetic SPECT #2 FWHM =11.91mm, σ_{noise}^2=100	7.80	24.91	f=1.12 M_{max}= 27.90	28.74 (f_c=3.68)	27.78	FWHM $_{est}$ =11.91mm K=97.65
Real SPECT	4.46	19.82	f=1.40 M_{max}= 27.74	10.38 (f_c=2.33)	27.64	FWHM $_{est}$ =13.11mm K=1562.5

Table 1: Summary of Experiment Results

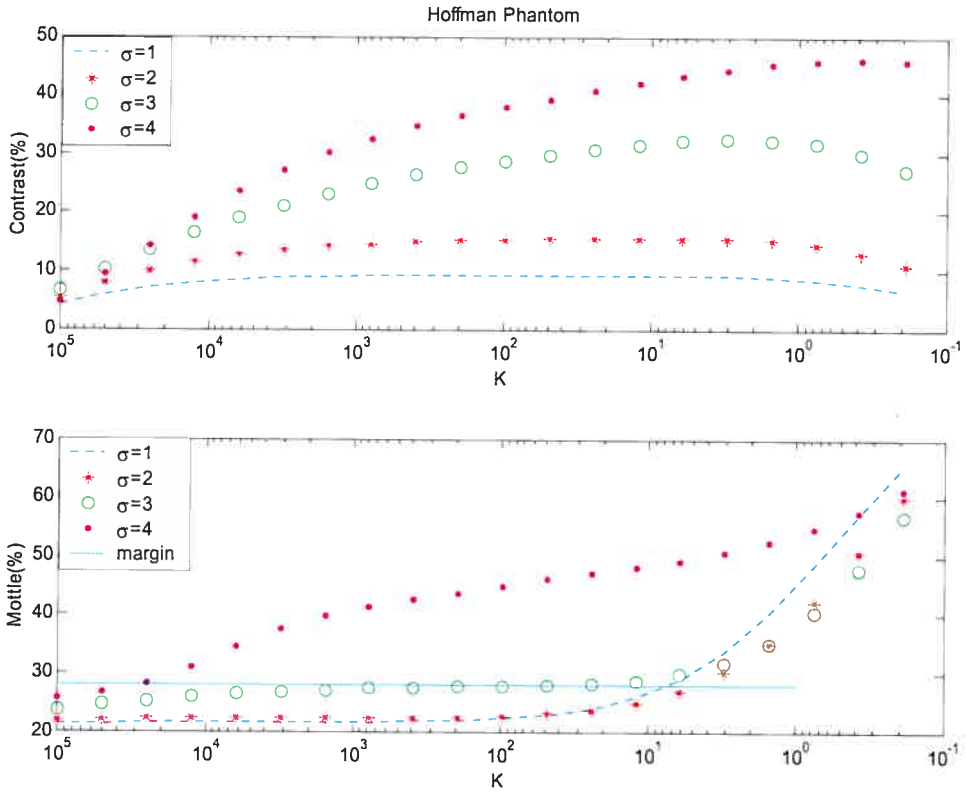

Figure 22 : Synthetic SPECT #2. (Up) Contrast vs. K with different σ in voxel. (Low) Mottle vs. K with different σ in voxel (1 voxel =1.69 mm and FWHM = 3.97 mm).

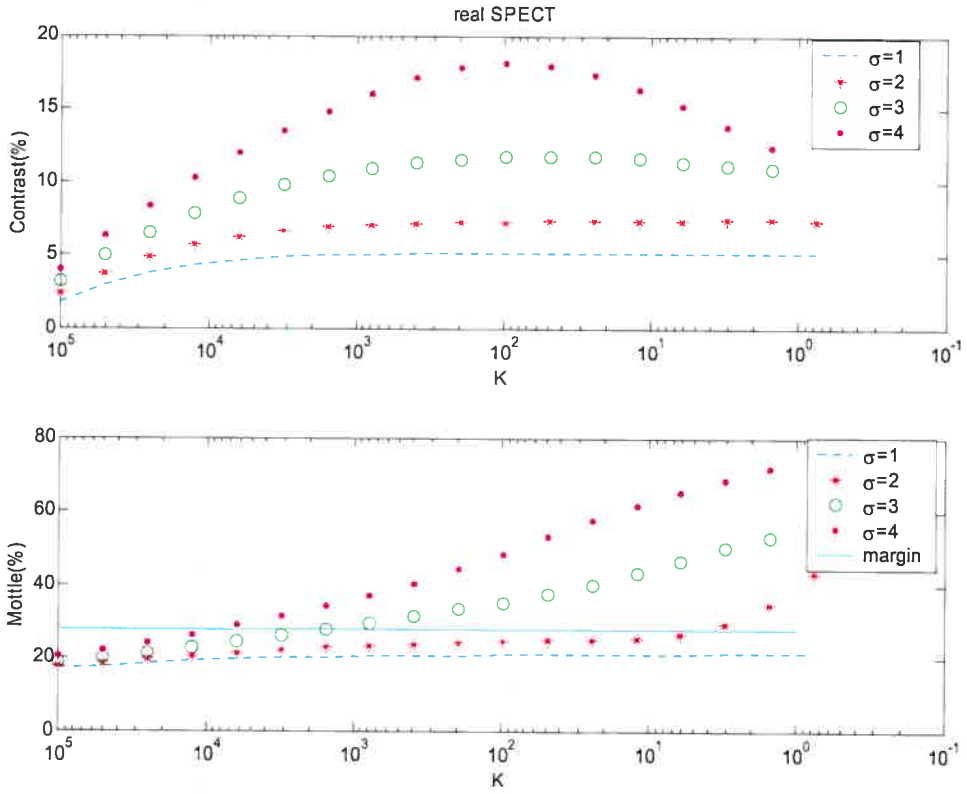

Figure 23: Real SPECT. (Up) Contrast vs. *K* with different σ in voxel. (Low) Mottle vs. *K* with different σ in voxel (1 voxel=1.86mm and FWHM = 4.38 mm).

For the restoration of the real brain SPECT, as Fig. 21(b) shows, the resulting image improves the contrast significantly by a factor of 2.33 (from 4.46% to 10.38%), while the mottle is increased just by a factor of 1.39 (from 19.82% to 27.64%). As a result of contrast improvement, the SPECT image after restoration provides much more details than the original one. The estimated PSF width and noise variance for this case are 13.11 mm FWHM and 1562.5 respectively, so we can say that the SPECT image is quite blurry and very noisy.

Figure 22 gives the relationships between contrast/mottle and the estimated value K with different values of PSF (σ in voxel) for the synthetic SPECT #2. Similarly, Fig. 23 is for the real SPECT image. From these figures, we can find that the contrast of the estimated images first increases, then becomes flat, and finally decrease as the constant K decreases, while the mottle always increases. Obviously, a higher contrast is with a

higher PSF (σ), e.g. 4 voxels in both figures, however, the mottle curves with higher PSF (σ) exceed the margin very quickly. Therefore, our method automatically takes a solution considering both contrast and mottle conditions.

It should be noted that the maximum margin among the three situations is set to 1.4, which is still considered acceptable when the contrast has been improved significantly (for example by a factor of 2) [WLOLF85].

The reference image takes an important role in our adaptive Wiener filtering processing because it can provide *a priori* information for the true scene. The different choices of parameters in the preprocessing programs may or may not affect the final results.

For the registration program *alignlinear*, if we replace the smoothing factor FWHM 8mm×8mm×8mm by 6mm×6mm×6mm or 10mm×10mm×10mm, or increase the threshold (t1) to 60 for the SPECT image, only minor changes will appear in the reference image, and none of them has an influence on the final estimates of the PSF width (σ) and the power spectrum of noise (K) for the adaptive Wiener filter, that is, we get the same results, $\sigma = 3$ (13.11 mm FWHM) and $K = 1562.5$ as in section 4.1 for the real SPECT image.

However, changes in the segmentation processing do make the adaptive Wiener filter generate different results. For example, when combining the two segmented images (GM and WM regions) into one file, if a voxel belonging to both regions is considered in the WM region instead of the GM region, the adaptive Wiener filter will choose the combination of $\sigma = 4$ voxels (15.88 mm FWHM) and $K = 12500$ to produce an estimate, which further smoothes the SPECT image. In this case, because the gray matter is a very thin layer in the brain, we must give it priority over the white matter, otherwise, the segmentation image will be less accurate.

As for the adaptive Wiener filter, two start values (σ_0 and K_0) for the PSF width and the power spectrum of noise respectively as well as the iterative step value K_{step} for updating the power spectrum of noise, have to be initialized. Usually, σ_0 is equal to 1 voxel (3.97 mm or 4.37 mm FWHM, depending on image voxel sizes) and K_0 is any big

number, such as 10^5. The choice of K_0 should be large enough. In addition, the power spectrum of noise K varies widely, hence we can not update it linearly, that is, we have to use $K = K/ K_{step}$ instead of $K = K + K_{step}$. It is evident that with a bigger step the program execution time is less. However, the restored image quality may not be improved optimally.

For the definition of the contrast, a weighted average contrast considering different interfaces between GM and WM, or WM and CSF, or GM and background, such as, $\overline{C} = \alpha(1 - \frac{m_{WM}}{m_{GM}}) + \beta(1 - \frac{m_{CSF}}{m_{WM}}) + \gamma(1 - \frac{m_{background}}{m_{GM}})$ may give a more accurate result.

Comparing the restored synthetic and real brain SPECT images, we can easily find that the former results are better than the later one. This is because *a priori* information about the true image is exactly known for Hoffman phantom and only pseudo-prior knowledge is used for SPECT restoration.

Chapter 5

Conclusion

We have proposed an adaptive Wiener filter that uses a reference image produced by a higher resolution brain MRI volume to provide *a priori* information for the brain SPECT image, based on the assumption that the PSF of the SPECT imaging is a Gaussian function with an unknown standard deviation and the system noise is AWGN. Then according to the contrast-mottle criterion, the algorithm calculates the best combination of the two parameters of the Wiener filter (the PSF width and the constant power spectrum density of noise), and finally restores the SPECT image.

Our experiment results prove that in the context of biomedical imaging, anatomical image such as MRI can provide *a priori* information for functional image such as SPECT.

Our adaptive Wiener filter can automatically choose the best combination of its parameters due to the application of the contrast-mottle criterion.

Our method does significantly improve the contrast and sharpness of synthetic and real SPECT image in clinic while keeping amplification of noise under acceptable level. The important point is that this filter has a high tolerance to noise.

Notice that the degradation model used by the adaptive Wiener filter assumes that noise is additive while in reality it is a multiplicative Poisson process. Nevertheless, the results with real SPECT/MRI data are visually impressive. It seems that at the high count level used in SPECT, the difference between (multiplicative) Poisson and (additive) Gaussian noise does not affect significantly the efficiency of the algorithm.

Some ideas for future work on this topic include:

* Build a user-friendly interface that will be helpful for the end-users, such as physicians and clinicians.

* Conduct clinical studies, for example epileptic studies. In these studies, the restored SPECT will be used to detect the focus of epileptic seizure in the region of the temporal lobe and perform Receiver Operator Characteristic (ROC) analysis [HM82][HM83] to measure the results of diagnosis with and without using our method.

References

[ABTA00] American Brain Tumor Association, "Facts and Statistics," Des Plaines, IL, 2000.

[AH77] H. C. Andrews and B. R. Hunt, "Digital Image Restoration," Englewood Cliffs, NJ: Prentice-Hall, 1977.

[APTA00] American Parkinson's Disease Association, "Personal Communication," October 10, 2000 based on figures from 1991. Silver Spring, MD.

[Bat82] R. H. T. Bates, "Astronomical speckle imaging," Phys Rep., vol. 99(4), pp. 203-97, Oct. 1982.

[BB73] V. A. Brookeman, and T. J. Bauer, "Collimator performance for scintillation camera systems," J. Nucl. Med. 14, pp 21-25, 1973.

[BGK98] R. Brookmeyer, S. and G. C. Kawas, "Projections of Alzheimer's disease in the United States and the public health impact of delaying disease onset," Am. J. Public Health 88, pp 1337-1342, 1998.

[BK97] M.R. Banham, and A. K. Katsaggelos, "Digital image restoration", IEEE Signal Processing Magazine, pp 24-41, Mar. 1997.

[BPLM97] M. H. Bourguignon, E. K. J. Pauwels, C. Loc and B. Maziere, "Iodine-123 labelled radiopharmaceuticals and single-photon emission tomography: a natural liaison," Eur. J. Nucl. Med., 24, pp 331-334, 1997.

[Can76] M. Cannon, "Blind deconvolution of spatially invariant images blurs with phase," IEEE Trans Acoust, Speech, Signal Processing, vol. 24(1), pp.58-63, Feb. 1976.

[Cat01] A. M. Catafau, "Brain SPECT in clinical practice Part I: Perfusion," J. Nucl. Med. 42 pp 259-271, 2001.

[CBMS04] G. D. Cascino, J. R. Buchalter, B. P. Mullan and E. L. So, "Ictal SPECT in Nonlesional Extratemporal Epilepsy", Epilepsia, 45(Suppl. 4):pp 32-34, 2004.

[Cha91] B. Chalmond, "PSF estimatioin for image deblurring," CVFIP: Graphical Models and Image Processing, vol. 53(4), pp.364-372, July 1991.

[CTE91] M. M. Chang, A. M. Tekalp and A. T. Erdem, "Blur identification using the bispectrum, " IEEE Trans Signal Processing, vol. 39(10), pp.2323-2325, Oct. 1991.

[Cit31] P. van Cittert, "Zum Einfluß der Spaltbreite auf die Intensitatsverteilung in Spektrallinien II," Zeitschrift fur Physik 69, 298–308, 1931.

[CC1898] P. Curie, and M. Curie, "Sur une nouvelle substance fortement radio-active, contenue dans la pechblende," Comptes rendus de l'Académie des Sciences, Paris, vol. 127, pp. 1215-1217, 26 December 1898.

[EBMTH88] A. C. Evans, C. Beil, S. Marrett, C. J. Thompson, and A. Hakim, "Anatomical–functional correlation using an adjustable MRI-based region of interest atlas with positron emission tomography," J. Cereb. Blood Flow Metab. 8 pp 513–30, 1988.

[FM91] R. Fabian and D. Malah, "Robust identification of motion and out-of-focus blur parameters from blurred and noisy images," CVFIP: Graphical Models and Image Processing, vol. 53(5), pp.403-412, Sept. 1991.

[FHRH04] J. B. Frederick, T. S. Harris, C. A. Roney and L. S. Hynan, "Differential Diagnosis Between Alzheimer's and Frontotemporal Disease by the Posterior Cingulate Sign", The Journal of Uuclear Medicine, Vol. 45, No. 5, pp 771-774, May 2004.

[Fri72] B. Frieden, "Restoring with maximum likelihood and maximum entropy," Journal of the Optical Society of America, 62 pp 511–518, 1972.

[FTG98] E. C. Frey, B. M. W. Tsui and G. T. Gullberg, "Improved estimation of the detector response function for converging beam collimator," Phys. Med. Biol. 43: 941-950, 1998.

[GTMPB88] D. R. Gilland, B. M. W. Tsui, W. H. McCarthy, J. R. Perry, and J. Berg. "Determination of the optimum filter function for SPECT imaging," J. Nucl. Med. 29, pp 643-650, 1988.

[GW87] R. C. Gonzalez, P. Wintz, "Digital image processing," Addison-Wesley Publishing Company, 1987.

[Had23] J. Hadamard, "Lectureson the Cauchy problem in linear partial differential equations," Yale University Press, 1923.

[HCDM90] E. J. Hoffman, P. D. Cultler, W. M. Digby and J. C. Mazziotta, "3-D Phantom to simulate cerebral blood flow and metabolic images for PET," IEEE Trans. On Nuclear Science, Vol. 37, No. 2 April 1990.

[HCJD] T. Hurtut, F. Cheriet, J. Joncas, and J. Dansereau, "Enhancement and segmentation of scar color images after a scoliosis surgery," Proc. VIIth Digital Image Computing: Techniques and Application, December 2003.

[HH94] M. Hanke and P.C. Hansen, "Regularization methods for large-scale problems," Surveys Math., 253-315, 1994.

[HHCGCBSG91]D. L. G. Hill, D. J. Hawkes, J. E. Crossman, M. J. Gleeson, T. C. S. Cox, E. E. C. M. L. Bracey, A. J. Strong and P. Graves, "Registration of MR and CT images for skull base surgery using point-like anatomical features," Br. J. Radiol. 64 1030–5, 1991.

[HM82] J. A. Hanley, and B. J. McNeil, "The meaning and use of the area under a receiver operating characteristic (ROC) curve," Radiology, 143:29-36, 1982.

[HM83] J. A. Hanley, and B. J. McNeil, "A method of comparing the areas under receiver operating characteristic curves derived from the same cases," Radiology, 148:839-843 1983.

[Hun73] B. R. Hunt, "The application of Constrained Least Squares Estimation to Image Restoration by Digital computer," IEEE Trans. Comput. Vol. C-22, no. 9 pp 805-812, 1973.

[Jay68] E. T. Jaynes. "Prior Probabilities," IEEE Trans. on Systems Science and Cybernetics, SSC-4, 227. 1968.

[KE63] D.E. Kuhl and R.Q. Edwards, "Image separation radioisotope scanning," Radiol, vol 80, pp. 653-662, 1963.

[KH96] D Kundur and d Hatzinakos, "Blind Image Deconvolution", IEEE Signal Processing Magazine, pp 43~64 , May 1996.

[Kin03] M. A. King. Project: "Digital Restoration of SPECT Images for Tumor Detection., Academic Radiology," Vol 10, Issue 9, pp 1079-1080, September 2003.

[LPCC88] D. N. Levin, C. A. Pelizzari, G. T. Y. Chen, C.-T. Chen and M. D. Cooper, "Retrospective geometric correlation of MR, CT, and PET images," Radiology 169 pp 817–23, 1988.

[Luc74] L. B. Lucy, "An iterative technique for the rectification of observed distribution," Astronomical Journal, vol 79, p. 745, June 1974.

[MBWMB96] T. M. Muir, A. Bradley, S. F. Wood, G. D. Murray, and M. J. Brodie, "An audit of treated epilepsy in Glasgow," West of Scotland Epilepsy Research Group. Seizure 5(1), pp 41–46, 1996.

[MD79] C. E. Metz, and K. Doi, "Transfer function analysis of radiographic imaging," Phys Med Biol 24 pp 1079-1106, 1979.

[Mig03] M. Mignotte, the course of "Digital image processing", 2003.

[Mil70] K. Miller, "Least squares methods for ill-posed problems with a prescribed bound," SIAM J. Math. Anal., 1 , pp. 52–74, 1970.

[MM00] M. Mignotte, and J. Meunier, "Three-dimensional blind deconvolution of SPECT images," IEEE Trans. Biomedical Engineering, vol. 47, pp. 274-280, Jan. 2000.

[MV98] J. B. Antoine Maintz, and M. A. Viergever, "A survey of Medical Image Registration, " Medical Image Analysis; 2:1-36, 1998.

[NPF98] National Parkinson Foundation, "What the Patient Should Know," Miami, FL, 1998.

[PPFJCR01] D. Pareto, J. Pavia, C. Falcon, I. Juvelles, A. Cot, and D. Ros, "Characterisation of fan-beam collimators," Eur. J. Nucl. Med. 28 pp 144-149, 2001.

[PTVF92] W. H. Press, S. A. Teukolsky, W. T. Vetterling and B. P. Flannery "Numerical Recipes in C: The Art of Scientific Computing," 2nd edition (Cambridge: Cambridge University Press), 1992.

[Ric72] W. H. Richardson, "Bayesian-based iterative method of image restoration," J. Opt. Soc. Am. Journal of the Optical Society of America, 62, pp. 55-59, 1972.

[RRPP02] F. Rooms , M. Ronsse , A. Pizurica , and W. Philips, "PSF estimation with application in autofocus and image restoration," Proc. IEEE Benelux Signal Processing Symposium (SPS-2002), Leuven, Belgium, March pp 21–22, 2002.

[RSNA02] RSNA 88th Scientific Assembly and Annual Meeting of the Radiological Society of North America, Abstract 897, Presented, Dec. 3, 2002.

[Smi02] S. M. Smith, "Fast robust automated brain extraction. Human Brain Mapping," 17(3) pp 143-155. 2002.

[Ste01] L Stefanovic, "The beginnings and development of diagnostic imaging in Nuclear Medicine," Med. Pregl.; 54(5-6), pp 289-96, May-Jun 2001.

[Wag03] H. N. Wagner, "Hal Anger: Nuclear Medicine's Quiet Genius," Nucl. Med., Vol. 44, No. 11, pp 26N~28N, 34N, Nov. 2003.

[WCM92] R. P. Woods, S. R. Cherry and J. C. Mazziotta, "Rapid Automated Algorithm for Aligning and Reslicing PET Images," J. Comput. Assist. Tomogr. 16(4) pp 620-633, 1992.

[WLOLF85] S. Webb, A. P. Long, R. J. Ott, M. O. Leach, and M. A. Flower, "Constrained deconvolution of SPECT liver tomograms by direct digital image restoration," Med, Phys., vol. 12, no. 1, pp 53-58 , 1985.

[WMC93] R. P. Woods, J. C. Mazziotta and S. R. Cherry, "MRI-PET registration with automated algorithm," J. Comput. Assist. Tomogr. 17 536–46, 1993.

[WST98] H. Wallace, S. Shorvon, and R. Tallis, "Age-specific incidence and prevalence rates of treated epilepsy in an unselected population of 2,052,922 and age-specific fertility rates of women with epilepsy," Lancet 352, pp 1970–1973, 1998.

Web Sites

[AB05] R. Ashby, and V. Bridge, University Of Leeds, last updated, 2005, http://www.leeds.ac.uk/

[ADERC05] Alzheimer's Disease Education and Referral Center, active in 2005, http://www.alzheimers.org/index.html

[AE93] Access Excellence, sponsored by The National Health Museum, launched in 1993, http://www.accessexcellence.org/AE/AEC/CC/radioactivity.html

[AF99] R. Abe, S. S. Furuie, 1999, The Research and Development Group of the Herat Instutute, University of São Paulo Medical School Hospital, http://www.incor.usp.br/spdweb/tomo2.html

[AIR02] Automated Image Registration, founded by R. P. Woods, last modified in 2002, http://bishopw.loni.ucla.edu/AIR5

[AM99] Aunt Minnie, founded by P. Berman in 1999, http://www.auntminnie.com/index.asp?sec=ref&sub=ncm&pag=cns&itemid=53715

[BL04] Berkeley Lab, University of California, last updated in 2004, http://www.lbl.gov/abc/Basic.html

[DICOM04] Digital Imaging and Communications in Medicine, last updated in 2004, http://medical.nema.org/

[DSC03] Data Spectrum Corporation, last updated in 2003, http://www.spect.com/pub/Hoffman_3D.doc.pdf

[FCA2001] Family Caregiver Alliance, prepared in 2001, http://www.caregiver.org/caregiver/jsp/content_node.jsp?nodeid=438&expandnodeid=480

[FCMC02] S. Frost, P. Crawford, S. Mera, and B. Chappell, "National Statement of Good Practice for the Treatment and Care of People who have Epilepsy," Joint Epilepsy Council. 2002, http://www.jointepilepsycouncil.org.uk

[IJ04] Image Processing and Analysis in Java, at Research Services Branch, last modified in 2004, http://rsb.info.nih.gov/ij/

[Nob05] Nobelprize, The Noble Foundation, last modified in 2005, http://nobelprize.org/physics/laureates/1903/becquerel-bio.html

[Ror04] C. Rorden, MRIcro, School of Psychology, University of Nottingham, 2004, http://www.psychology.nottingham.ac.uk/staff/cr1/mricro.html

[San03] Albert Cot Sanz, "Absolute quantification in brain SPECT imaging", 2003, http://www.tdx.cesca.es/TESIS_UPC/AVAILABLE/TDX-0227104-131558/TESI.pdf

[SNM05] The Society of Nuclear Medicine, last modified in 2005, http://interactive.snm.org/index.cfm?PageID=1107&RPID=1307

[Wik05] Wikipedia, last modified in 2005, http://en.wikipedia.org/wiki/Principle_of_maximum_entropy